Aerospace Science and Technology 179 (2026) 113305

Contents lists available at ScienceDirect

Aerospace Science and Technology

journal homepage: www.elsevier.com/locate/aescte

Airship dynamics in a tethered docking maneuver

Carlo E.D. Riboldi *, Alessandro Croce, Francesco A.C. Pagani, Hui He, Giorgio Bortolini

Department of Aerospace Science and Technology, Politecnico di Milano, via La Masa, 34, Milano, 20156, Italy

A R T I C L E I N F O

Communicated by Dr. Mehdi Ghoreyshi

Keywords:
Airship
Tether cable
Tethered flight
Tether force
Docking maneuver
Flight control
Lighter than air
LTA

A B S T R A C T

In the context of the currently growing interest of industry and research towards the field of controlled airships, in particular in association to unmanned flight, the availability of methods and tools for the analysis of specific maneuvers faced by airships over their typical mission profile constitutes a relevant asset. The inherent dynamics of this class of flying vehicles, dominated by buoyancy and by the aerodynamics of their envelope, produces a peculiar response especially in terminal maneuvers and in the docking phase. The latter is often carried out with the help of tethering cables, which further influence the dynamic behavior of the airship, in a way depending on the number and physical characteristics of the cables, the tethering points on board, the rewind velocity, etc. For a better understanding of the airship response in this type of maneuver, mid-fidelity dynamic models of both the airship and tethering cables are employed in this research. They are applied in a first stage to understand the effect of tethering cables on the dynamics of the airship, through a detailed linear analysis. The latter is performed in a parameterized fashion, studying the effect of different parameters on dynamic stability. Then the analysis of the outcome of fully non-linear simulations of an airship anchored to the ground via a rewinding tethering cable is proposed, showing the effect of different simple control logics on the behavior of the airship during an idealized docking manevuer. The proposed modeling and analysis methods allow to efficiently study the behavior of steerable lighter-than-air vehicles in terminal maneuvers, with a detail sufficient for airship design and characterization phases, also making for an interesting asset in the compliance-checking phase with respect to regulatory requirements.

1. Introduction

As reported by the specialized recent literature dedicated to the topic [1], as well as the recent record-setting flights in the most challenging high-altitude scenario [2], airships are currently opening interesting technological niches in the aeronautical field. Thanks to the relaxation of layout criteria, enabled by the adoption of high thrust-to-weight electric motors in lieu of piston power, novel configurations are being explored for lighter-than-air (LTA) flight [3–5], especially in combination with the small-size and light-payload unmanned type of mission [6–8]. On the other end of the technological spectrum, airships are under consideration as alternatives to fixed-wing platforms in very challenging high-altitude pseudo-satellite missions, where the chance to relocate the machine as well as of recovering its payload put them in an advantageous position compared to space satellites [2,9].

Beside a design problem, now covered by an abundant literature documenting several different sizing techniques [10–17], airships invariably pose some issues through their complex in-flight behavior. To study and forecast their response in flight as well as in terminal maneuvers close to the ground, much attention has been devoted in the past to set up mid-fidelity models [18–22]. Notably, these models invariably consider the airship as rigid, characterized by a slender (also, ideally axial-symmetric) envelope and tail layout, and with an assigned positions of the centers of buoyancy and gravity, as well as of the thrusters. They employ typically a hybrid approach for the computation of aerodynamic forces, where potential flow solutions are assumed to recover aerodynamic lift and moment components due to the envelope (reflecting the classical approach originally encoded by Munk [23]), whereas some model for viscous forces, also entailing cross-flow effects due to possible high angle of attack operations, uncommon on aircraft but achievable on airships, is employed in association to the envelope as well as the tail fins [24,25]. Such inherently non-linear aerodynamic models may be employed to obtain linearized representations of the dynamics of the airship in proximity to an equilibrium point. However, such linearized models have a limited validity for simulation purposes, on account of the significant non-linearity of airship aerodynam-

* Corresponding author.
E-mail address: carlo.riboldi@polimi.it (C.E.D. Riboldi).
URL: www.riboldiresearch.net (C.E.D. Riboldi)

https://doi.org/10.1016/j.ast.2026.113305
Received 30 March 2026; Received in revised form 26 May 2026; Accepted 21 July 2026
Available online 24 July 2026

Nomenclature

$\boldsymbol{A}$	State matrix of twelve-dimensional system
$\boldsymbol{AP}_i$	Ground anchor point for ith cable
$\boldsymbol{B}$	Center of buoyancy
$\boldsymbol{C}$	Reference point on tether cable
$\boldsymbol{G}$	Center of gravity
$\boldsymbol{F}_i, \tilde{\boldsymbol{F}}_i$	Tension vector at $\boldsymbol{TP}_i$, at generic coordinate of ith tether cable
$\boldsymbol{I}_{(\cdot)}, \boldsymbol{0}_{(\cdot)}$	Identity matrix, null matrix
$\boldsymbol{J}^i_{\boldsymbol{P}}$	Inertia tensor wrt. point $\boldsymbol{P}$
$\tilde{\boldsymbol{K}}$	Twelve-dimensional stiffness matrix
$\tilde{\boldsymbol{M}}$	Twelve-dimensional mass matrix
$\boldsymbol{M}^a_{\boldsymbol{P}}$	Generalized apparent mass matrix wrt. point $\boldsymbol{P}$
$\boldsymbol{M}^i_{\boldsymbol{P}}$	Generalized mass matrix wrt. point $\boldsymbol{P}$
$\boldsymbol{P}^{\mathcal{B}}_{321_0}$	Matrix linking $\Delta\boldsymbol{e}^{\mathcal{B}}_{321}$ to $\Delta\dot{\boldsymbol{e}}^{\mathcal{B}}_{321}$
$\boldsymbol{R}^{\mathcal{A}}_{\mathcal{A}\to\mathcal{B}}$	Rotation tensor from reference $\mathcal{A}$ to $\mathcal{B}$ by components in reference $\mathcal{A}$
$\boldsymbol{S}_{\boldsymbol{P}}$	Static moment wrt. point $\boldsymbol{P}$
$\boldsymbol{S}^{\mathcal{B}}_{321}$	Matrix linking $\dot{\boldsymbol{e}}^{\mathcal{B}}_{321}$ to $\boldsymbol{\omega}^{\mathcal{B}}_{\mathcal{B}}$
$\boldsymbol{T}_i, T_i$	Thrust vector and intensity for ith thruster
$\boldsymbol{TP}_i$	On-board tether point for ith cable
$\boldsymbol{U}$	Control sensitivity matrix of twelve-dimensional system
$\boldsymbol{W}^{(\cdot)}_{\boldsymbol{P},s}, \boldsymbol{W}^{(\cdot)}_{\boldsymbol{P},\delta}$	Generalized force sensitivity matrices to state and control (six rows)
$\tilde{\boldsymbol{W}}^{(\cdot)}_{\boldsymbol{P},s}, \tilde{\boldsymbol{W}}^{(\cdot)}_{\boldsymbol{P},\delta}$	Sensitivity matrices to state and control (twelve rows)
$\boldsymbol{b}_1, \boldsymbol{b}_2, \boldsymbol{b}_3$	Unit vectors of the three axes of reference $\mathcal{B}$
$\boldsymbol{c}_1, \boldsymbol{c}_2, \boldsymbol{c}_3$	Unit vectors of the three axes of reference $\mathcal{C}$
$\boldsymbol{e}^{\mathcal{B}}_{321}$	Array of Euler angles of body reference wrt. ground reference
$\boldsymbol{f}^{(\cdot)}$	Active force
$\boldsymbol{g}, g$	Gravitational acceleration vector, modulus
$\boldsymbol{h}_{\boldsymbol{C}}$	Unit vector with $\boldsymbol{v}^a_{\boldsymbol{C}}$
$\boldsymbol{i}_1, \boldsymbol{i}_2, \boldsymbol{i}_3$	Unit vectors of the three axes of reference $\mathcal{I}$
$\boldsymbol{j}$	Unit vector between cable extremities
$\boldsymbol{j}'_{\boldsymbol{C}}$	Component of $\boldsymbol{j}$ normal to $\boldsymbol{h}_{\boldsymbol{C}}$
$\boldsymbol{k}_{\boldsymbol{C}}$	Unit vector normal to $\boldsymbol{j}$
$\boldsymbol{l}^{(\cdot)}, \boldsymbol{l}^{(\cdot)}_{\boldsymbol{C}}$	Cable external load vector (or load at point $\boldsymbol{C}$) per unit length
$\boldsymbol{m}^{(\cdot)}_{\boldsymbol{P}}$	Active moment wrt. point $\boldsymbol{P}$
$\boldsymbol{q}_{(\cdot)}$	Position vector of generic point wrt. origin of body reference
$\boldsymbol{r}^{(\cdot)}_{\boldsymbol{P}}$	Generalized force vector wrt. point $\boldsymbol{P}$
$\boldsymbol{s}$	Twelve-dimensional state array
$\boldsymbol{t}_i$	Thrust nominal unit vector for ith thruster
$\boldsymbol{v}_{\boldsymbol{P}}$	Velocity of point $\boldsymbol{P}$ wrt. ground observer (ground speed)
$\boldsymbol{v}_W$	Wind speed vector measured by ground observer
$\boldsymbol{v}^a_{(\cdot)}$	Airspeed at generic point
$\boldsymbol{v}^{a'}_{(\cdot)}$	Component of $\boldsymbol{v}^a_{(\cdot)}$ normal to $\boldsymbol{j}$
$\boldsymbol{w}_{\boldsymbol{P}}$	Generalized state vector wrt. point $\boldsymbol{P}$
$\boldsymbol{x}_{(\cdot)}$	Position vector of generic point wrt. origin of ground reference
$\boldsymbol{z}$	Generic three-dimensional vector
$\boldsymbol{\delta}$	Array of controls
$\boldsymbol{\delta}^a$	Array of aerodynamic surface controls
$\boldsymbol{\delta}^t$	Array of throttle settings
$\boldsymbol{\omega}_{\mathcal{B}}$	Rotational speed of reference $\mathcal{B}$ wrt. ground observer
ADC	Actuator duty cycle
$C_{d,c}, C_{d,l}$	Cross-flow and longitudinal drag coefficients of cable
D_t	Diameter of cable
E_{δ_T}	Energy associated to thrust control action
FR	Fineness ratio of envelope
$J^a_{(\cdot)}$	Component of apparent inertia
K_0	Nominal stiffness of cable
L_{t_i}	Length of ith cable
$\bar{L}_{t_i}$	Non-dimensional length parameter of ith cable
$N_{(\cdot)}$	Number of thrusters (T), cables (C), controls (δ)
RoC	Rate of climb
U, V, W	Components of $\boldsymbol{v}_{\boldsymbol{P}}$ in body reference ($\mathcal{B}$)
e_i	Elongation of ith cable
$k_{(\cdot)}, k'$	Munk's factors
m	Mass
p, q, r	Components of $\boldsymbol{\omega}_{\mathcal{B}}$ in body reference ($\mathcal{B}$)
u	Catenary solution
$y_i, \bar{y}_i$	Generic abscissa, abscissa of $\boldsymbol{TP}_i$ extremity along $\boldsymbol{c}_i$
$\Delta(\cdot)$	Quantity change or perturbation
Λ	Catenary solution parameter
Ψ	Rewind rate
Ω	Catenary solution parameter
α_C	Reference angle of attack of cable
β_i	Nominal slope of cable
δ_{T_i}	Throttle setting of ith thruster
$\varepsilon_{(\cdot)}$	Positional error
ϑ	Second rotation angle in 3-2-1 Euler's sequence (pitch angle)
$\kappa_{(\cdot)}$	Control gain
ρ	Volumetric density of air
ρ_t	Linear density of cable
φ	Third rotation angle in 3-2-1 Euler's sequence (roll angle)
χ	Horizontal misalignment angle
ψ	First rotation angle in 3-2-1 Euler's sequence (yaw angle)
$\mathcal{B}, (\cdot)^{\mathcal{B}}$	Body reference, by components in body reference
$\mathcal{C}, (\cdot)^{\mathcal{C}}$	Cable local reference, by components in cable local reference
$\mathcal{I}, (\cdot)^{\mathcal{I}}$	Ground reference (inertial), by components in ground reference
$\mathcal{V}$	Volume
$(\cdot)_0$	Value in reference condition (trim)
$\dot{(\cdot)}$	Time derivative

ics and the pronounced dependence of their dynamic response on the airspeed [26].

Models in this class, capable of efficiently support simulation campaigns while capturing most of the flight dynamics of the airship (while leaving out typically deformation and aero-elastic effects, which is starting to receive attention after some years of neglect in the airship domain [27,28]), can be profitably employed for carrying out control design and testing, thus facing a relevant issue associated to airship operations, especially when unmanned flight is of interest and a high level of automation in flight is pursued. The literature on control with application to airship flight is rich, concentrating however mostly on the management of flight operations [29–34], including hovering [5]. Little attention has been devoted to the analysis of docking maneuvers [35]. In this context, it is worth mentioning that, as typical to aircraft, regulations (still in an embryonic stage, concerning unmanned LTA platforms [36]) shall in the near future pose some clear constraints, thus on the one hand helping designers through quantitative indications, and on the other requiring some precise assessment of the performance of an airship in a docking maneuver.

As a matter of fact, currently the docking maneuver is carried out either manually for smaller platforms, or in a tethered condition on larger transports. Tethered flight has been since long of major interest for lighter-than-air platforms. The concept of tethered aerostats and airships has received extensive attention in the past [37–40], and more recently especially for applications in the higher layers of the atmosphere. Much literature has been devoted to the analysis of a fully-tethered mission, where the airship is conceived to make use of the tether as a major means of control, and concentrating on the phases of the flight of the greatest interest for design, i.e. ascent/descent and especially cruise [41–43]. In conjunction with mid-to-high altitude operations, also relatively high-fidelity models of the tether, based on a discretization of its properties along its length (and the introduction of a correspondingly higher number of positional states), have been studied. This approach is in order to capture the reaction of the system to the far-from-uniform wind conditions met by the tether along its span in high-altitude missions, and to accurately account for low-frequency dynamic effects (i.e., induced also by tether inertia), which are particularly relevant for longer, hence heavier, tether cables.

Compared to the literature on tethered flight, the topic of tethered docking has received much less attention. Just like for any other flying machine, this terminal phase is inherently risky, hence, as pointed out, it is likely to be in the focus of a dedicated regulatory effort targeting the electrically-propelled, low-weight airship drone class [36]. Furthermore, the automatically regulated actuation of the tether cable and the cooperation of the airship in the docking phase are enablers in the achievement of a fully-automatic docking capability.

To the aim of developing a better understanding of the dynamic behavior displayed by an airship in a tethered docking phase, a purpose-designed mid-fidelity model is introduced, by merging in a single suite the non-linear model for a rigid airship in flight and a numerically efficient model for a tethering cable [44,45], capable of capturing the zero-frequency tension and deformation of the cable with a fast and accurate procedure. While moving to a higher level of accuracy compared to the preliminary forays in this domain [35] (which made use of a reduced-order linearized model for the airship), the model proposed in this paper does not renounce to numerical simplicity and execution speed, thus bending itself to an use in parameterized analyses. This approach has been purposely pursued in order to make this model useful for airship designers and control designers as well, in a typical virtual testing campaign for certification compliance verification.

The aim of the paper is two-fold. After introducing the dynamic models for the airship and tether in detail, including a rigorous vector-calculus characterization of the tether cable static deformation model which allows for a pitfall-free and accurate implementation, the potential of the ensuing model suite is shown by analyzing a realistic specimen scenario in detail. In this way, the potential of the model in assisting computational dynamic performance evaluations is coupled with the analysis of a case study worth investigation, thus studying in detail the behavior of an airship in tethered flight. Many diverse parameterized analyses are proposed in this paper. A mid-sized unmanned airship is considered for the task, tethered by a lightweight anchoring cable. A first parameterized analysis is carried out on the free response of the tethered system, performed through linear analysis in trimmed conditions, showing the effect of key parameters featured in the design of the airship/tether cable and in the testing scenario (e.g. the wind intensity). Subsequently, the dynamic analysis of a docking maneuver is proposed, performed through non-linear runs of the simulator for a tethered airship, considering as parameters the wind (including side gusts), and assuming different control logics, finally ranked in terms of their ability to reduce the docking time while mitigating tension at the tether-airship interface, thus avoiding potential tear of the airship envelope attachment and cable overstress. The sensitivity of the model synthesized here to the parameters of the equilibrium problem, as well as those of different control laws, shows that this model may constitute a helpful tool in the design and testing of new airships and control algorithms, complementing the modeling tools currently available for a corresponding analysis of free (i.e. untethered) flight.

2. Modeling approach

A mid-fidelity non-linear model suitable for the analysis of airship flight dynamics has been introduced and validated in previous works by the authors [4,5,17]. It will be briefly reviewed here. Conversely, particular attention will be given to the model considered for the analysis of a tether cable, originating mostly from the approach proposed in [44], which has been coupled to the airship flight dynamics model in this research. The complete derivation of a linearized model, drawn from the assembled models of the airship and tether cable, will follow the discussion of the non-linear one.

2.1. Non-linear model for airship dynamics

The dynamic balance equations of an airship in flight can be written according to a generalized agnostic tensor form, in particular considering the generic point $\boldsymbol{P}$ for expressing inertial properties and for measuring active moments,

$$\left(\boldsymbol{M}^i_{\boldsymbol{P}} + \boldsymbol{M}^a_{\boldsymbol{P}}\right)\dot{\boldsymbol{w}}_{\boldsymbol{P}} + \boldsymbol{w}_{\boldsymbol{P}_\times}\boldsymbol{M}^i_{\boldsymbol{P}}\boldsymbol{w}_{\boldsymbol{P}} = \boldsymbol{r}^a_{\boldsymbol{P}} + \boldsymbol{r}^b_{\boldsymbol{P}} + \boldsymbol{r}^p_{\boldsymbol{P}} + \boldsymbol{r}^g_{\boldsymbol{P}} + \boldsymbol{r}^t_{\boldsymbol{P}}. \tag{1}$$

In Eq. (1), the left-hand side (l.h.s.) represents the inertial reaction of the system. Let a body reference centered in point $\boldsymbol{P}$ be defined so that its unit vectors, associated with its three orthonormal axes $\boldsymbol{b}_1, \boldsymbol{b}_2, \boldsymbol{b}_3$, point respectively to the nose of the airship, to the right and to the bottom as in Fig. 1 (as typical also to the domain of winged aircraft dynamics [46,47]).

Then the generalized mass matrices in Eq. (1) write in body components $(\cdot)^{\mathcal{B}}$

$$\boldsymbol{M}^{i,\mathcal{B}}_{\boldsymbol{P}} = \begin{bmatrix} m\boldsymbol{I}_3 & \boldsymbol{S}^{\mathcal{B}^T}_{\boldsymbol{P}} \\ \boldsymbol{S}^{\mathcal{B}}_{\boldsymbol{P}} & \boldsymbol{J}^{\mathcal{B}}_{\boldsymbol{P}} \end{bmatrix}, \qquad \boldsymbol{M}^{a,\mathcal{B}}_{\boldsymbol{P}} = \boldsymbol{M}^{a,\mathcal{B}}_{\boldsymbol{P}}\left(\mathcal{V}, FR, \boldsymbol{q}_{\boldsymbol{B}}\right), \tag{2}$$

wherein m is the mass of the airship, $\boldsymbol{I}_3$ is a 3-by-3 identity, $\boldsymbol{S}^{\mathcal{B}}_{\boldsymbol{P}}$ and $\boldsymbol{J}^{\mathcal{B}}_{\boldsymbol{P}}$ respectively the static moment and moment of inertia of the airship wrt. point $\boldsymbol{P}$ in body components, $\mathcal{V}$ is the airship volume, FR the fineness ratio of the airship envelope, and $\boldsymbol{q}_{\boldsymbol{B}}$ represents the position vector of the center of buoyancy $\boldsymbol{B}$ with respect to point $\boldsymbol{P}$. Concerning $\boldsymbol{M}^{a,\mathcal{B}}_{\boldsymbol{P}}$, the expression in Eq. (2) is an implicit generalization of the more familiar writing often adopted when $\boldsymbol{P} = \boldsymbol{B}$, such that $\boldsymbol{M}^{a,\mathcal{B}}_{\boldsymbol{B}} = \mathrm{diag}\left(k_1\mathcal{V}, k_2\mathcal{V}, k_3\mathcal{V}, 0, k' J^a_2, k' J^a_3\right)$, where J^a_2 and J^a_3 represent the inertia of the mass of air displaced by the external volume of the airship around the pitch and yaw axes (i.e., along $\boldsymbol{b}_2$ and $\boldsymbol{b}_3$ respectively), often referred to as apparent inertia, and k_1, k_2, k_3, k' are Munk's factors for the airship [23]. The generalized state array, in body components, is

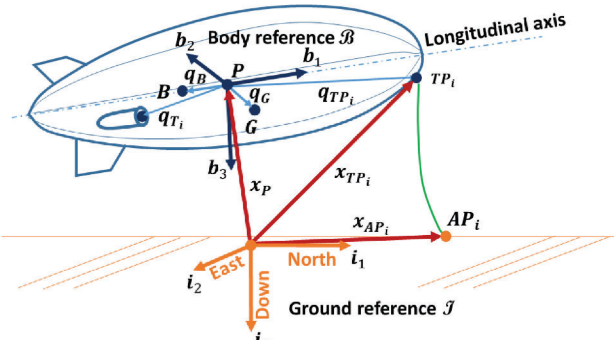

Fig. 1. Definitions of ground and body references, and of position vectors employed in the model.

defined as

$$\boldsymbol{w}_{\boldsymbol{P}}^{\mathcal{B}} = \left\{ \begin{array}{c} \boldsymbol{v}_{\boldsymbol{P}}^{\mathcal{B}} \\ \boldsymbol{\omega}_{\mathcal{B}}^{\mathcal{B}} \end{array} \right\} = \{U, V, W, p, q, r\}^T. \tag{3}$$

In Eq. (3), $\boldsymbol{v}_{\boldsymbol{P}}^{\mathcal{B}}$ represents the velocity vector of point $\boldsymbol{P}$ with respect to a ground-fixed reference $\mathcal{I}$, assumed inertial, with unit vectors $\boldsymbol{i}_1$ and $\boldsymbol{i}_2$ pointing North and East respectively, and $\boldsymbol{i}_3$ pointing down (see Fig. 1). Similarly, $\boldsymbol{\omega}_{\mathcal{B}}^{\mathcal{B}}$ represents the rotational speed vector of the body-attached reference $\mathcal{B}$ with respect to the ground-fixed reference $\mathcal{I}$. Both vectors in Eq. (3) have been expressed in body components. The operator $\times\!\!\!\!\!\times$ is defined such that when applied to a generic six-dimensional vector $\boldsymbol{z}$, defined as the assembly of two three-dimensional vectors $\boldsymbol{z} = \left\{z_1, z_2\right\}^T$ (i.e., exactly like $\boldsymbol{w}_{\boldsymbol{P}}$ in Eq. (3)), it is such that

$$z_{\times\!\!\!\!\times} = \left[\begin{array}{cc} z_{2_\times} & \mathbf{0} \\ z_{1_\times} & z_{2_\times} \end{array} \right], \tag{4}$$

wherein $(\cdot)_\times$ represents the skew-symmetric form of a vector.

The right-hand side (r.h.s.) of Eq. (1) is composed of five generalized forcing terms, respectively representing aerodynamics ($\boldsymbol{r}_{\boldsymbol{P}}^a$), buoyancy ($\boldsymbol{r}_{\boldsymbol{P}}^b$), propulsion ($\boldsymbol{r}_{\boldsymbol{P}}^p$), gravity ($\boldsymbol{r}_{\boldsymbol{P}}^g$) and tether tension ($\boldsymbol{r}_{\boldsymbol{P}}^t$). Each generalized forcing term conveys two vectors in three-dimensional space, namely a force and moment wrt. point $\boldsymbol{P}$, so that

$$\boldsymbol{r}_{\boldsymbol{P}}^{(\cdot)} = \left\{ \begin{array}{c} \boldsymbol{f}^{(\cdot)} \\ \boldsymbol{m}_{\boldsymbol{P}}^{(\cdot)} \end{array} \right\}. \tag{5}$$

It can be noted that, by adopting the agnostic form in Eq. (1), the specification of the dynamic balance typical to a specific craft or another only requires the corresponding writing of a suitable set of generalized forces on the r.h.s., and possibly the specification of the displaced mass and inertia term on the l.h.s., when this is non-negligible (as for airships or submarines). In this way, from the same baseline writing, different models can be obtained, for example, for an airship, a rotor-craft or a winged aircraft, either with or without a tether acting on the machine (in the latter case, $\boldsymbol{r}_{\boldsymbol{P}}^t = \mathbf{0}$).

Considered from an implementation stand-point, Eq. (1) is composed of six scalar first-order non-linear differential equations. However, as known, the forcing terms on the r.h.s. depend on the state array $\boldsymbol{w}_{\boldsymbol{P}}$, but as well on additional quantities. These include the orientation angles of the body in space, represented by three Euler angles $\boldsymbol{e}_{321}^{\mathcal{B}} = \{\varphi, \vartheta, \psi\}^T$, which are invariably imported at least by gravity, as well as the positional information wrt. the ground reference $\mathcal{I}$, wrapped in the position vector $\boldsymbol{x}_{\boldsymbol{P}}$ of point $\boldsymbol{P}$, imported in the equations by tether force, as will be detailed in the next paragraphs. The position vector, written by components in a ground reference $\mathcal{I}$ as $\boldsymbol{x}_{\boldsymbol{P}}^{\mathcal{I}}$, conveys three scalar variables. Furthermore, control variables may impact aerodynamic forces (i.e., through the commanded deflection of control surfaces) and propulsion forces (through the throttle setting of each thruster). Considering controls as assigned quantities, it is however clear that the balance of equations vs. unknowns requires the addition of six relations flanking the dynamic balance in Eq. (1), linking the six additional scalar variables in $\boldsymbol{e}_{321}^{\mathcal{B}}$ and $\boldsymbol{x}_{\boldsymbol{P}}^{\mathcal{I}}$ to the components of the array $\boldsymbol{w}_{\boldsymbol{P}}^{\mathcal{B}}$, yielding an overall balanced system of twelve equations in twelve differential unknowns. The first set of three kinematic relations is constituted by the usual link [46,47] between the components of $\boldsymbol{\omega}_{\mathcal{B}}^{\mathcal{B}} = \{p, q, r\}^T$ and the time derivative of the elements of $\boldsymbol{e}_{321}^{\mathcal{B}}$, such that

$$\dot{\boldsymbol{e}}_{321}^{\mathcal{B}} = \boldsymbol{S}_{321}^{-1^{\mathcal{B}}} \boldsymbol{\omega}_{\mathcal{B}}^{\mathcal{B}}, \text{ with } \boldsymbol{S}_{321}^{\mathcal{B}} = \left[\begin{array}{ccc} 1 & 0 & -\sin\vartheta \\ 0 & \cos\varphi & \sin\varphi\cos\vartheta \\ 0 & -\sin\varphi & \cos\varphi\cos\vartheta \end{array} \right]. \tag{6}$$

The second set of three kinematic equations is constituted by the link between the time derivatives of the position vector in ground components, $\dot{\boldsymbol{x}}_{\boldsymbol{P}}^{\mathcal{I}}$, and the components of the translational velocity in body components, $\boldsymbol{v}_{\boldsymbol{P}}^{\mathcal{B}} = \{U, V, W\}^T$, which can be written via the corresponding rotation matrix from reference $\mathcal{I}$ to $\mathcal{B}$ (the representation is invariant in either of the two [47]), yielding

$$\dot{\boldsymbol{x}}_{\boldsymbol{P}}^{\mathcal{I}} = \boldsymbol{R}_{\mathcal{I}\to\mathcal{B}}^{\mathcal{I}} \boldsymbol{v}_{\boldsymbol{P}}^{\mathcal{B}}, \text{ with } \boldsymbol{R}_{\mathcal{I}\to\mathcal{B}}^{\mathcal{I}} =$$

$$\left[\begin{array}{ccc} \cos(\vartheta)\cos(\psi) & \sin(\varphi)\sin(\vartheta)\cos(\psi) - \cos(\varphi)\sin(\psi) & \cos(\varphi)\sin(\vartheta)\cos(\psi) + \sin(\varphi)\sin(\psi) \\ \cos(\vartheta)\sin(\psi) & \sin(\varphi)\sin(\vartheta)\sin(\psi) + \cos(\varphi)\cos(\psi) & \cos(\varphi)\sin(\vartheta)\sin(\psi) - \sin(\varphi)\cos(\psi) \\ -\sin(\vartheta) & \sin(\varphi)\cos(\vartheta) & \cos(\varphi)\cos(\vartheta) \end{array} \right]. \tag{7}$$

Eqs. (1), (6), (7) make for twelve scalar first-order non-linear differential relations in the twelve scalar unknowns, wrapped in the augmented state array $\boldsymbol{s} = \left\{\boldsymbol{w}_{\boldsymbol{P}}^{\mathcal{B}}, \boldsymbol{e}_{321}^{\mathcal{B}}, \boldsymbol{x}_{\boldsymbol{P}}^{\mathcal{I}}\right\}^T$.

2.1.1. Models for the generalized forces for an untethered airship

In this section the modeling approach adopted for the generalized forces due to aerodynamics, buoyancy, gravity and propulsion will be defined. For aerodynamics, since no novelty has been introduced with respect to the existing literature [4,5,17,18], the rather articulated model encoded in this component will be only outlined.

Aerodynamics. The aerodynamic model considered in this research for an airship is described in the theory developed by Munk, Jones and DeLaurier [18,23]. Considering the envelope of the airship, a discretization along the longitudinal axis is carried out, producing a set of discrete elements (*slices*, according to Jones and DeLaurier nomenclature). For each discrete element, a method for computing three local contributions to aerodynamic force values and the corresponding contributions to moment is implemented [18]. Potential flow is employed for lift forces and the ensuing moment. For this computation, the method accounts for the local value of the airspeed vector, itself due to the linear velocity and rotational rate of the body, respectively $\boldsymbol{v}_{\boldsymbol{P}}^{\mathcal{B}}$ and $\boldsymbol{\omega}_{\mathcal{B}}^{\mathcal{B}}$ defined as in Eq. (3), according to an hypothesis of rigid body, and to the local acceleration vector. The aerodynamic model estimates the drag according to an attached flow and a cross-flow effect [18,24], thus allowing one to effectively capture the behavior of the airship also for a high angle of attack [20], which might be encountered on an airship more easily than on a winged aircraft, for instance when maneuvering in near-hover conditions [5]. The contribution of the envelope to the overall aerodynamic actions on the airship is extended from the nose to a longitudinal station defined in proximity of the leading edge of the root airfoil of the tails, from where the flow is assumed to be dominated by the action of the tail fins.

The fins are treated each according to a simple lumped model, where aerodynamic lift, drag and moment coefficient sensitivities, specified as known parameters, are employed to compute aerodynamic forces and torque due to attached flow and cross-flow components [18,24,25], and the knowledge of the positions of the aerodynamic center and cross-flow force center of each fin with respect to the measuring point $\boldsymbol{P}$ allows one to compute the overall moment due to the aerodynamic forces. The local angle of attack and sideslip are computed based on the actual positioning and incidence angle of the fin with respect to the airship body reference.

Notably, in presence of a non-null wind, a distinction between the airspeed and the airship velocity has to be made. Let vector $\boldsymbol{v}_W$ identify the wind velocity vector, i.e. the speed of the wind with respect to a ground observer. Then the velocity vector $\boldsymbol{v}_{\boldsymbol{P}}$ of point $\boldsymbol{P}$ on the airship, which in the aeronautical domain is typically referred to as *ground speed* and taken by components in $\mathcal{B}$ represents a component of the airship state (Eq. (3)), is related to the *airspeed* vector $\boldsymbol{v}_{\boldsymbol{P}}^a$ by the definition $\boldsymbol{v}_{\boldsymbol{P}} = \boldsymbol{v}_W + \boldsymbol{v}_{\boldsymbol{P}}^a$. Additionally, a non-null wind vector $\boldsymbol{v}_W$ produces a dependence of the aerodynamic action from the attitude angles in $\boldsymbol{e}_{321}^{\mathcal{B}}$ (which is seldom accounted for when describing flight dynamics).

The generalized aerodynamic force in body components can be expressed in general as a function $\boldsymbol{r}_{\boldsymbol{P}}^a = \boldsymbol{r}_{\boldsymbol{P}}^a\left(\boldsymbol{w}_{\boldsymbol{P}}, \boldsymbol{e}_{321}^{\mathcal{B}}, \delta^a\right)$, where the dependence on $\boldsymbol{e}_{321}^{\mathcal{B}}$ is specifically activated by a non-zero $\boldsymbol{v}_W$, and δ^a conveys the control variables impacting aerodynamic forces (typically, the deflection of control surfaces on the trailing edge of the fins).

Buoyancy and gravity. Buoyancy and gravity are both strictly related to the gravitational acceleration vector $\boldsymbol{g}$. By components in the ground reference $\mathcal{I}$, the respective forces can be computed as

$$\boldsymbol{f}^{b,\mathcal{I}} = -\rho\mathcal{V}\boldsymbol{g}^{\mathcal{I}} = \begin{Bmatrix} 0 \\ 0 \\ -\rho\mathcal{V}g \end{Bmatrix}, \quad \boldsymbol{f}^{a,\mathcal{I}} = m\boldsymbol{g}^{\mathcal{I}} = \begin{Bmatrix} 0 \\ 0 \\ mg \end{Bmatrix}, \tag{8}$$

where ρ represents the density of the air. The corresponding moments are due to the moment arm between the generic measuring point $\boldsymbol{P}$ and, respectively, the center of buoyancy $\boldsymbol{B}$, where the buoyancy force is centered (i.e., where the distribution of buoyancy force produces no moment), and the center of gravity $\boldsymbol{G}$, where gravity force is centered. These are represented by the relative position vectors $\boldsymbol{q_B}$ and $\boldsymbol{q_G}$, pointing the respective points from point $\boldsymbol{P}$, and yielding

$$\boldsymbol{m}_{\boldsymbol{P}}^{b,\mathcal{I}} = \boldsymbol{q}_{\boldsymbol{B}}^{\mathcal{I}} \times \boldsymbol{f}^{b,\mathcal{I}}, \quad \boldsymbol{m}_{\boldsymbol{P}}^{g,\mathcal{I}} = \boldsymbol{q}_{\boldsymbol{G}}^{\mathcal{I}} \times \boldsymbol{f}^{g,\mathcal{I}}. \tag{9}$$

In Eq. (9) the specification of $\boldsymbol{q}_{\boldsymbol{B}}^{\mathcal{I}}$ and $\boldsymbol{q}_{\boldsymbol{G}}^{\mathcal{I}}$ by components in the ground reference $\mathcal{I}$ is possible by preliminarily assigning these vectors by components in the body reference $\mathcal{B}$ (where they will be typically constant and more practical to assign, for a known mass and volume distribution), and by turning them into ground components via a change of reference operation, as $\boldsymbol{q}_{(\cdot)}^{\mathcal{I}} = \boldsymbol{R}_{\mathcal{I}\to\mathcal{B}}^{\mathcal{I}} \boldsymbol{q}_{(\cdot)}^{\mathcal{B}}$. Conversely, the forces and moments in Eqs. (8) and (9) shall be turned into body components, to be put in the dynamic balance in Eq. (1), expressed in reference $\mathcal{B}$. This can be performed with the inverse transformation, i.e. $\boldsymbol{f}^{(\cdot),\mathcal{B}} = \boldsymbol{R}_{\mathcal{I}\to\mathcal{B}}^{\mathcal{I}^T} \boldsymbol{f}^{(\cdot),\mathcal{I}}$, and similarly for moment. Notably, the dependence of buoyancy force an moment on the components of the augmented state will be only with respect to the attitude angles $\boldsymbol{e}_{321}^{\mathcal{B}}$ appearing in the rotation matrix $\boldsymbol{R}_{\mathcal{I}\to\mathcal{B}}^{\mathcal{I}}$ (Eq. (7)). Therefore, in general $\boldsymbol{r}_{\boldsymbol{P}}^{b} = \boldsymbol{r}_{\boldsymbol{P}}^{b}\left(\boldsymbol{e}_{321}^{\mathcal{B}}\right)$ and $\boldsymbol{r}_{\boldsymbol{P}}^{g} = \boldsymbol{r}_{\boldsymbol{P}}^{g}\left(\boldsymbol{e}_{321}^{\mathcal{B}}\right)$.

Propulsion. Propulsion actions are modeled introducing a force vector for each ith thruster, as

$$\boldsymbol{T}_i = T_i\left(\delta_{T_i}, \boldsymbol{v}_{T_i}^a, \rho\right)\boldsymbol{t}_i, \tag{10}$$

wherein $T_i\left(\delta_{T_i}, \boldsymbol{v}_{T_i}^a, \rho\right)$ is the intensity of the thrust force, modeled as a known function of the throttle setting δ_{T_i} and airspeed pertaining to the motor position in the layout of the airship $\boldsymbol{v}_{T_i}^a$, and of the density of air ρ. The term $\boldsymbol{t}_i$ represents a unit vector pointing in the nominal direction of thrust, and depends on the specific airship design and thruster layout. The position of the thruster in the airship layout can be specified with a position vector from point $\boldsymbol{P}$, namely $\boldsymbol{q}_{\boldsymbol{T}_i}$. The generalized propulsion force $\boldsymbol{r}_{\boldsymbol{P}}^{p}$ can be expressed easily in body components as

$$\boldsymbol{r}_{\boldsymbol{P}}^{p,\mathcal{B}} = \sum_{i=1}^{N_T} \begin{Bmatrix} \boldsymbol{I}_3 \\ \boldsymbol{q}_{\boldsymbol{T}_{i\times}}^{\mathcal{B}} \end{Bmatrix} \boldsymbol{T}_i^{\mathcal{B}}, \tag{11}$$

where N_T is the number of thrusters. Notably, the expression of $\boldsymbol{t}_i^{\mathcal{B}}$ by components in the body reference, goes through a constant rotation when the mutual attitude of the thruster is fixed with respect to the airship (i.e. defined by fixed vertical and side-ward incidences within the layout of the airship), whereas that rotation may be specified as a function of time when thrust vector control is implemented. Of the airship states in $\boldsymbol{s}$, the generalized propulsion force is a function of $\boldsymbol{v}_{\boldsymbol{P}}^{\mathcal{B}}$ and $\boldsymbol{\omega}_{\mathcal{B}}^{\mathcal{B}}$ through the local airspeed $\boldsymbol{v}_{T_i}^a$, so that in general $\boldsymbol{r}_{\boldsymbol{P}}^{p} = \boldsymbol{r}_{\boldsymbol{P}}^{p}\left(\boldsymbol{v}_{\boldsymbol{P}}, \boldsymbol{\omega}_{\mathcal{B}}, \boldsymbol{\delta}^t\right)$, where $\boldsymbol{\delta}^t$ conveys the throttle settings δ_{T_i} of the N_T thrusters.

2.1.2. *Modeling of the tether cable tension*

As specified in the introduction, the approach outlined in [44] and [45], originally developed for tethered kites, has been employed as a baseline for the computation of the tension at the tether point $\boldsymbol{TP}_i$ of an ith tether cable on the airship. Starting from the original theoretical development found in the literature, a model has been elaborated in this research to include it within the tensor calculus approach employed for the formulation of airship dynamics. An advantage of this formulation is the ability of a corresponding implementation to seamlessly treat totally generic maneuvers, without caring specifically on a case-by-case basis for the provenience of the wind, the mutual positioning of the extremities of the tether cable, etc.. This makes an ensuing simulation code totally general with respect to the simulated condition, significantly less error-prone and inherently more robust (i.e., virtually pitfall-free) than case-tailored formulations. Furthermore, the elemental approach in the modeling of each item producing force (or moment), like for the thrusters (see previous paragraph), allows to easily replicate the same computations when more elements of the same class are present in the simulation scenario (e.g., when more cables are at hand).

The model employed in this research defines three working conditions for the tether cable, based on the elongation of the cable e. This can be defined starting from the distance between the tether cable extremities, namely the on-board tether point $\boldsymbol{TP}_i$ and the ground anchor point $\boldsymbol{AP}_i$ for the ith tether cable, and from its nominal length L_{t_i}, so that $e_i = \frac{\left\|\boldsymbol{x}_{\boldsymbol{TP}_i} - \boldsymbol{x}_{\boldsymbol{AP}_i}\right\|}{L_{t_i}}$. These working conditions can be synthetically described as follows.

1. *Elongation is such that it does not stimulate an elastic force*. Numerically, $e_i < e_{i,c}$, where $e_{i,c}$ may be typically slightly below unity. In these conditions the intensity and direction of the tension force is dictated by the solution of the catenary deformation of the tether. This case will be detailed later in this section.
2. *Elongation is dominated by elastic force*. Numerically, $e_i > e_{i,e}$, where $e_{i,e}$ is typically slightly above unity. In these conditions, the cable is assumed to behave like an elastic system according to Hooke's law, with tension acting on the airship aligned with $\left(\boldsymbol{x}_{\boldsymbol{AP}_i} - \boldsymbol{x}_{\boldsymbol{TP}_i}\right)$, yielding

$$\boldsymbol{F}_i = K_0\left(e_i - e_{i,c}\right) \cdot \frac{\boldsymbol{x}_{\boldsymbol{AP}_i} - \boldsymbol{x}_{\boldsymbol{TP}_i}}{\left\|\boldsymbol{x}_{\boldsymbol{AP}_i} - \boldsymbol{x}_{\boldsymbol{TP}_i}\right\|} \tag{12}$$

   where K_0 represents an axial stiffness coefficient for the fully stretched cable.
3. *Elongation is such to stimulate a non-negligible elastic force*. Numerically this condition is treated with a transition model, which applies for a range $e_{i,c} \le e_i \le e_{i,e}$. A linear jointing law has been employed in this research, where the tension is defined based on the value of the catenary solution $\boldsymbol{F}_{i,c}$ computed at $e_i = e_{i,c}$ and the elastic solution $\boldsymbol{F}_{i,e}$ computed for $e_i = e_{i,e}$, so that

$$\boldsymbol{F}_i = \boldsymbol{F}_{i,c} + \left(e_i - e_{i,c}\right) \cdot \frac{\boldsymbol{F}_{i,e} - \boldsymbol{F}_{i,c}}{\left(e_{i_e} - e_{i_c}\right)}. \tag{13}$$

Considering now the model which applies in the mostly relevant case 1. just mentioned, a major hypothesis underlying the computation of tension force at any station within the cable is the uniformity of the load per unit length $\boldsymbol{l_C}$ (the nature of point $\boldsymbol{C}$ will be clarified in the next lines), which is induced by gravity and aerodynamic actions along the cable length. This hypothesis strongly simplifies the computation of the static solution for the deformation and for the tension of the cable, which is possible by solving a single scalar algebraic implicit equation. Clearly, a model based on this approach will capture only the static solution of cable deformation and tension, which is interesting only for static or slowly-evolving dynamic maneuvers of a tethered airship. However, this should suffice for the analysis of a slow docking maneuver, for example. Furthermore, the rather low intensities of mass-related (i.e. induced by gravity and inertia) and aerodynamic actions on the tether cable of an airship, compared to the forces acting on the airship itself, allow one to assume that the forces borne by the cable and injected in the tethered airship system will be generally less significative than the intensity of the force system originating from the airship (i.e. due to thrust, the buoyancy and weight of the airship, its own aerodynamics and inertia). However, the direction of the tension along the cable, capable of influencing the dynamics of the airship, is clearly a function of its own

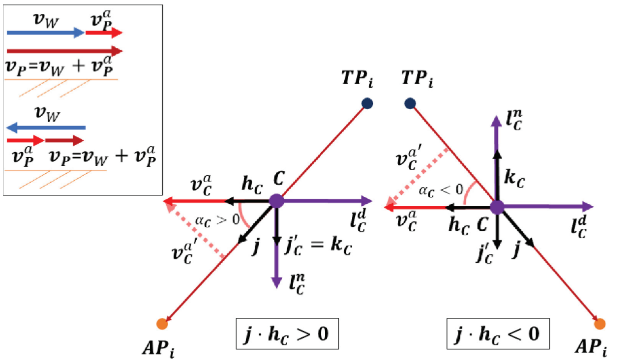

Fig. 2. Definition of aerodynamic load on a cable. Left and right: Two alternative cases of mutual orientation of the airspeed vector $\boldsymbol{v}_C^a$ and cable attitude unit vector $\boldsymbol{j}$. Top-left box: Relationship between ground speed $\boldsymbol{v}_P$, wind speed $\boldsymbol{v}_W$ and airspeed $\boldsymbol{v}_P^a$ in downwind and upwind conditions (top and bottom respectively).

characteristics and local loads. Therefore it deserves a modeling effort, of the same level of accuracy as that adopted for airship flight dynamics. A suitable model is represented by the static solution, as pointed out [44,45]. The load due to gravity on the cable is defined as

$$
\boldsymbol{l}^{g,\mathcal{I}} = \left\{ \begin{array}{c} 0 \\ 0 \\ g\rho_t \end{array} \right\}, \tag{14}
$$

where ρ_t represents the linear density of the cable. According to the definition in Eq. (14), this is generally uniform. Conversely, the aerodynamic load vector is generally non-uniform, since it will depend on the local airspeed at any given point along the cable, and on its angle with respect to the local direction of the cable. The model adopted here introduces a reference point $\boldsymbol{C}$ on the cable, where conceptually the local intensity and angle of the airspeed are representative of an average of the aerodynamic action on the cable. As a result, by computing the local aerodynamic forces at point $\boldsymbol{C}$, an average value of these forces can be defined for the cable, and employed as a uniform load to carry out the computation of the tension with the relatively straightforward procedure presented in the following. The aerodynamic action per unit length at the reference point $\boldsymbol{C}$ can be quantified conveniently by introducing firstly a unit vector $\boldsymbol{j}$ pointing from the tether point $\boldsymbol{TP}_i$ on the airship to the anchor point $\boldsymbol{AP}_i$ on ground (representing the opposite extremity of the cable), which is correspondingly defined as $\boldsymbol{j} = \left(\boldsymbol{x}_{\boldsymbol{AP}_i} - \boldsymbol{x}_{\boldsymbol{TP}_i}\right) / \left\|\boldsymbol{x}_{\boldsymbol{AP}_i} - \boldsymbol{x}_{\boldsymbol{TP}_i}\right\|$ (note this is the same appearing in Eq. (12)), as in Fig. 2.

Adopting a typical definition for aerodynamic drag, it is possible to assign its direction by introducing the unit vector $\boldsymbol{h}_C$ for the drag per unit length, as $\boldsymbol{h}_C = \boldsymbol{v}_C^a / \left\|\boldsymbol{v}_C^a\right\|$, where $\boldsymbol{v}_C^a$ is the airspeed vector at point $\boldsymbol{C}$. The drag force per unit length vector can be computed in ground components ($\mathcal{I}$) as

$$
\boldsymbol{l}_C^{d,\mathcal{I}} = -\frac{1}{2}\rho D_t \left(C_{d,c} \left| \sin^3 \alpha_C \right| + C_{d,l} \right) \left(\boldsymbol{v}_C^a \cdot \boldsymbol{v}_C^a \right) \boldsymbol{h}_C^{\mathcal{I}}, \tag{15}
$$

wherein D_t is the diameter of the cable, $C_{d,c}$ and $C_{d,l}$ are cable-specific drag force coefficients [24,44] (functions of the airflow Reynolds number). In Eq. (15) the local angle of attack α_C can be estimated by taking the component of the airspeed $\boldsymbol{v}_C^a$ along the direction of $\boldsymbol{j}$, i.e. $\boldsymbol{v}_C^{a\prime} = \boldsymbol{v}_C^a - \boldsymbol{j}\left(\boldsymbol{j} \cdot \boldsymbol{v}_C^a\right)$, and by computing the inverse tangent

$$
\alpha_C = \tan^{-1} \left(\frac{\left\| \boldsymbol{v}_C^{a\prime} \right\|}{\boldsymbol{v}_C^a \cdot \boldsymbol{j}} \right). \tag{16}
$$

The remaining component of aerodynamic force at point $\boldsymbol{C}$ is acting in a direction normal to that of the airspeed $\boldsymbol{v}_C^a$, and defined in space by the local direction of the airspeed wrt. the cable. The corresponding unit vector $\boldsymbol{k}_C$ is obtained by taking the component of $\boldsymbol{j}$ normal to the direction of the drag, i.e. $\boldsymbol{j}_C' = \boldsymbol{j} - \boldsymbol{h}_C \left(\boldsymbol{h}_C \cdot \boldsymbol{j}\right)$, and by computing the sign-assigning normalization

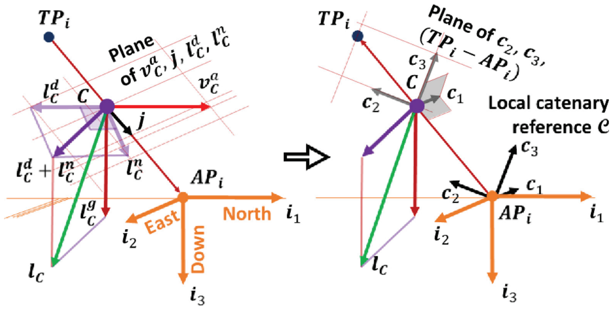

Fig. 3. Definition of local catenary reference $\mathcal{C}$, from loads and geometrical quantities.

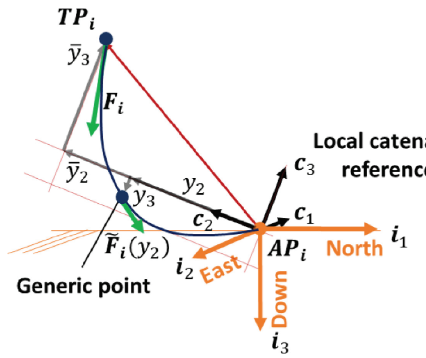

Fig. 4. Definition of local cable coordinates, employing the local catenary reference $\mathcal{C}$.

$$
\boldsymbol{k}_C = \operatorname{sign}\left(\boldsymbol{j} \cdot \boldsymbol{h}_C\right) \cdot \frac{\boldsymbol{j}_C'}{\left\| \boldsymbol{j}_C' \right\|}. \tag{17}
$$

Based on Eq. (17), it is easy to obtain the remaining aerodynamic load per unit vector, which in ground components can be computed as

$$
\boldsymbol{l}_C^{n,\mathcal{I}} = \frac{1}{2}\rho D_t \left(C_{d,c} \left| \sin^2 \alpha_C \cdot \cos \alpha_C \right| \right) \left(\boldsymbol{v}_C^a \cdot \boldsymbol{v}_C^a \right) \boldsymbol{k}_C^{\mathcal{I}}. \tag{18}
$$

Then the uniform load which the tether cable is assumed to be subject to is quantified in ground components as $\boldsymbol{l}_C^{\mathcal{I}} = \boldsymbol{l}^{g,\mathcal{I}} + \boldsymbol{l}_C^{d,\mathcal{I}} + \boldsymbol{l}_C^{n,\mathcal{I}}$. Now the solution of the static deformation and tension of a cable subject to this load can be computed based on a catenary model. Let the tether reference $\mathcal{C}$ be defined by the mutually-orthogonal unit vectors

$$
\boldsymbol{c}_3 = -\frac{\boldsymbol{l}_C}{\left\|\boldsymbol{l}_C\right\|}, \quad \boldsymbol{c}_1 = \frac{\left(\boldsymbol{x}_{\boldsymbol{TP}_i} - \boldsymbol{x}_{\boldsymbol{AP}_i}\right) \times \boldsymbol{c}_3}{\left\|\left(\boldsymbol{x}_{\boldsymbol{TP}_i} - \boldsymbol{x}_{\boldsymbol{AP}_i}\right) \times \boldsymbol{c}_3\right\|}, \quad \boldsymbol{c}_2 = \boldsymbol{c}_3 \times \boldsymbol{c}_1, \tag{19}
$$

forming a right-handed triad. Fig. 3 helps in capturing the identity and geometrical properties of the three unit vectors in Eq. (19).

By projecting the relative position vector of the tether point wrt. the anchor point $\left(\boldsymbol{x}_{\boldsymbol{TP}_i} - \boldsymbol{x}_{\boldsymbol{AP}_i}\right)$ in the local $\mathcal{C}$ reference, the three abscissas $\bar{y}_j = \left(\boldsymbol{x}_{\boldsymbol{TP}_i} - \boldsymbol{x}_{\boldsymbol{AP}_i}\right) \cdot \boldsymbol{c}_j$, $j = 1, \ldots, 3$ are defined, as shown in Fig. 4. The parameters $\bar{L}_{t,i} = \frac{\bar{y}_2}{L_{t,i}}$ and $\beta_i = \frac{\bar{y}_3}{\bar{y}_2}$ can be computed next, and employed to solve the implicit scalar equation

$$
u = \cosh^{-1} \left(u \frac{\bar{L}_{t,i}^2 - \beta_i^2}{2} + 1 \right)^2. \tag{20}
$$

To ensure robustness when implementing this model within a wrapping solver for airship dynamics, care should be taken in the numerical solution of Eq. (20), so as to steer a solution algorithm towards the only strictly positive solution among all possible, for instance by bounding the solution and properly selecting the initial guess above the minimum value of the associated residual function. From the solution of u, two additional parameters can be computed, namely

$$\Omega = \frac{\sqrt{u}}{\bar{y}_2}, \quad \Lambda = \frac{\bar{L}_{t_i} \sinh\left(\Omega \bar{y}_2\right) - \bar{y}_3 \cdot \left(\cosh\left(\Omega \bar{y}_2\right) - 1\right)}{2\cosh\left(\Omega \bar{y}_2\right) - 1}. \tag{21}$$

The catenary solution parameters in Eq. (21) can be finally employed for computing the solution of the static cable deformation and the tension along the cable, and specifically at its extremities. The deformed cable is by construction laid within the plane normal to $\boldsymbol{c}_1$, and such that it can be expressed as a function y_3 (i.e., a coordinate along $\boldsymbol{c}_3$) of an abscissa y_2 along $\boldsymbol{c}_2$, yielding

$$y_3 = \left(\bar{y}_3 + \Lambda\right)\frac{\sinh\left(\Omega y_2\right)}{\sinh\left(\Omega \bar{y}_2\right)} - \Lambda + \Lambda \frac{\sinh\left(\Omega\left(\bar{y}_2 - y_2\right)\right)}{\sinh\left(\Omega \bar{y}_2\right)}, \tag{22}$$

where it is apparent that the solution returns $y_3 = 0$ for $y_2 = 0$, representing the passage by the ground anchor point $\boldsymbol{AP}_i$, and $y_3 = \bar{y}_3$ for $y_2 = \bar{y}_2$, representing the passage by the on-board attachment point (airship tether point $\boldsymbol{TP}_i$). As for tension, the derivative of the previous expression wrt. the abscissa y_2 is required, yielding

$$y_3' = \frac{\mathrm{d}y_3}{\mathrm{d}y_2} = \frac{\Lambda\left(\Omega \cosh\left(\Omega y_2\right) - \Omega\cosh\left(\Omega\left(\bar{y}_2 - y_2\right)\right)\right) + \Omega \bar{y}_3 \cosh\left(\Omega y_2\right)}{\sinh\left(\Omega \bar{y}_2\right)}. \tag{23}$$

The tension, based on Eq. (23), just like the deformation from Eq. (22) can be evaluated in local coordinates ($\mathcal{C}$), at any point represented by the generic abscissa y_2 (Fig. 4), according to the definition

$$\tilde{\boldsymbol{F}}_i^{\mathcal{C}} = \left\{ \begin{array}{c} 0 \\ \frac{l_c \cdot c_3}{\Omega} \\ y_3'\left(y_2\right)\frac{l_c \cdot c_3}{\Omega} \end{array} \right\} \tag{24}$$

This allows one for instance to easily find the maximum value of the tension along the cable. However, of the greatest relevance for the dynamics of a tethered airship is the tension vector at the tether point $\boldsymbol{TP}_i$, which is obtained by evaluating Eq. (24) for $y_2 = \bar{y}_2$, yielding $\boldsymbol{F}_i^{\mathcal{C}} = \tilde{\boldsymbol{F}}_i^{\mathcal{C}}\left(\bar{y}_2\right)$ (see Fig. 4).

In order to obtain the tension components in the airship body reference $\mathcal{B}$, which is needed to compute the generalized action $\boldsymbol{r}_{\boldsymbol{P}}^t$ within the dynamic balance equations in the same reference as for all other actions, it is convenient to first express it by components in the ground reference, by exploiting the easy writing of the three unit vectors in Eq. (17) in reference $\mathcal{I}$. The explicit expression of $\boldsymbol{c}_3^{\mathcal{I}}$ can be obtained starting from $\boldsymbol{l}_{\boldsymbol{C}}^{\mathcal{I}}$, which is obtained from Eqs. (14), (15), (18). The position vector $\boldsymbol{x}_{\boldsymbol{AP}_i}$ is most naturally assigned in ground components, whereas the position vector $\boldsymbol{x}_{\boldsymbol{TP}_i}$ can be obtained by definition as $\boldsymbol{x}_{\boldsymbol{TP}_i} = \boldsymbol{x}_{\boldsymbol{P}} + \boldsymbol{q}_{\boldsymbol{TP}_i}$, where $\boldsymbol{q}_{\boldsymbol{TP}_i}$ represents the position of the tether point on board the airship from the measuring point $\boldsymbol{P}$ where the dynamic balance is expressed, and can be typically specified easily in constant body components (i.e., $\boldsymbol{q}_{\boldsymbol{TP}_i}^{\mathcal{B}}$). The latter expression in a ground reference yields $\boldsymbol{x}_{\boldsymbol{TP}_i}^{\mathcal{I}} = \boldsymbol{x}_{\boldsymbol{P}}^{\mathcal{I}} + \boldsymbol{R}_{\mathcal{I}\to\mathcal{B}}^{\mathcal{I}} \boldsymbol{q}_{\boldsymbol{TP}_i}^{\mathcal{B}}$. These observations in turns allow to obtain explicitly the components of $\boldsymbol{c}_2^{\mathcal{I}}$ and $\boldsymbol{c}_1^{\mathcal{I}}$, and to correspondingly build the rotation matrix $\boldsymbol{R}_{\mathcal{I}\to\mathcal{C}}^{\mathcal{I}} = \left[\boldsymbol{c}_1^{\mathcal{I}} | \boldsymbol{c}_2^{\mathcal{I}} | \boldsymbol{c}_3^{\mathcal{I}}\right]$. With the latter, the tension by components in the ground reference $\mathcal{I}$ is finally obtained as $\boldsymbol{F}_i^{\mathcal{I}} = \boldsymbol{R}_{\mathcal{I}\to\mathcal{C}}^{\mathcal{I}} \boldsymbol{F}_i^{\mathcal{C}}$. From this, the tension in body components is correspondingly computed as $\boldsymbol{F}_i^{\mathcal{B}} = \boldsymbol{R}_{\mathcal{I}\to\mathcal{B}}^{\mathcal{I}^T} \boldsymbol{F}_i^{\mathcal{I}}$.

Considering the general case where the airship is attached to more cables (indexed as ith), each associated to a tension $\boldsymbol{F}_i$ at the corresponding on-board tether point $\boldsymbol{TP}_i$, and that no moment is discharged by the cable at the level of the attachment, it is possible to define the action $\boldsymbol{r}_{\boldsymbol{P}}^t$ to fit in the dynamic balance in Eq. (1), in body reference, as

$$\boldsymbol{r}_{\boldsymbol{P}}^{t,\mathcal{B}} = \sum_{i=1}^{N_C} \left\{ \begin{array}{c} \boldsymbol{I}_3 \\ \boldsymbol{q}_{\boldsymbol{TP}_{i\times}}^{\mathcal{B}} \end{array} \right\} \boldsymbol{F}_i^{\mathcal{B}}, \tag{25}$$

where N_C is the number of tether cables attached to the airship.

Interestingly, the dependence of the tether generalized force is on all quantities in the array of states $\boldsymbol{s}$, whereas there is no direct action of the controls on it. In particular, velocity and rotational rate within $\boldsymbol{w}_{\boldsymbol{P}}$ produce an effect on the velocity of the tether point on board $\boldsymbol{TP}_i$, influencing the reference airspeed $\boldsymbol{v}_{\boldsymbol{C}}^a$ of a tether cable, whereas the attitude represented by $\boldsymbol{e}_{321}^{\mathcal{B}}$ and the position $\boldsymbol{x}_{\boldsymbol{P}}$ define the mutual position of the tether point on board with respect to the anchor point $\boldsymbol{AP}_i$ on ground. Therefore, formally $\boldsymbol{r}_{\boldsymbol{P}}^t = \boldsymbol{r}_{\boldsymbol{P}}^t\left(\boldsymbol{w}_{\boldsymbol{P}}, \boldsymbol{e}_{321}^{\mathcal{B}}, \boldsymbol{x}_{\boldsymbol{P}}\right)$.

2.2. Linearized model for airship dynamics

In order to carry out a linear analysis starting from the framework of the non-linear model employed in the previous section, an approach was selected where the reaction term on the l.h.s. of the dynamic balance equation (Eq. (1)), as well as the kinematic relations in Eqs. (6) and (7), are linearized analytically, yielding an explicit writing, outlined later in this section. Conversely, the r.h.s. of Eq. (1) is linearized numerically by employing a perturbation method. The latter is far more convenient than an analytic approach, on account of the extremely complex equations linking the states and controls to aerodynamic, propulsion and tether actions (whereas for buoyancy and gravity an analytic linearized expression could be worked out easily). Of course, a writing in states-space form could be also obtained, by deploying a perturbation method and computing $\dot{\boldsymbol{s}}$ directly, yielding the state and control sensitivity matrices, thus bypassing the analytic computation of the l.h.s. of the dynamic balance equations and of the kinematic relations. In this research, both ways have been tested for cross-validation, obviously getting the same results. The first (semi-analytic) way is presented here primarily to capture the effect of having the position of the measuring point $\boldsymbol{P}$ not coinciding with that of the center of gravity (which would yield some simplification, typical to the fixed-wing aeronautical domain [46]) or the center of buoyancy (which would produce some simplification as well, an approach often adopted when writing the equations of motion for airships [20]), and for showing the complete derivation of a linear form for kinematic equations, including Eq. (7) which is seldom treated in aeronautical flight dynamics problems, and is crucial when dealing with a tethered platform.

2.2.1. Reaction term in the dynamic balance equations

The linearization process for the dynamic balance equations in Eq. (1) starts from the substitution of a linear expansion of the solution $\boldsymbol{w}_{\boldsymbol{P}} = \boldsymbol{w}_{\boldsymbol{P}_0} + \Delta\boldsymbol{w}_{\boldsymbol{P}}$ on the l.h.s. and of the forcing terms $\boldsymbol{r}_{\boldsymbol{P}}^{(\cdot)} = \boldsymbol{r}_{\boldsymbol{P}_0}^{(\cdot)} + \Delta\boldsymbol{r}_{\boldsymbol{P}}^{(\cdot)}$ on the r.h.s.. Upon replacement in the dynamic balance equation and elimination of the identity representing equilibrium in the reference condition (i.e., those terms with subscript $(\cdot)_0$ only), it is possible to obtain the linear perturbation form of the dynamic balance equations,

$$\begin{aligned}\left(\boldsymbol{M}_{\boldsymbol{P}}^i + \boldsymbol{M}_{\boldsymbol{P}}^a\right)\Delta\dot{\boldsymbol{w}}_{\boldsymbol{P}} &+ \boldsymbol{w}_{\boldsymbol{P}_0} \times \boldsymbol{M}_{\boldsymbol{P}}^i \Delta\boldsymbol{w}_{\boldsymbol{P}} + \Delta\boldsymbol{w}_{\boldsymbol{P}} \times \boldsymbol{M}_{\boldsymbol{P}}^i \boldsymbol{w}_{\boldsymbol{P}_0} \\ &= \Delta\boldsymbol{r}_{\boldsymbol{P}}^a + \Delta\boldsymbol{r}_{\boldsymbol{P}}^b + \Delta\boldsymbol{r}_{\boldsymbol{P}}^g + \Delta\boldsymbol{r}_{\boldsymbol{P}}^p + \Delta\boldsymbol{r}_{\boldsymbol{P}}^t.\end{aligned} \tag{26}$$

Concentrating on the l.h.s., when leaving $\boldsymbol{P}$ as a generic position (i.e., not setting it as a special point like the center of gravity), the first term in Eq. (26) can be nonetheless easily written recurring to Eq. (2) (by components in a body reference), whereas the second and third terms yield

$$\begin{aligned}\boldsymbol{w}_{\boldsymbol{P}_0} \times \boldsymbol{M}_{\boldsymbol{P}}^i \Delta\boldsymbol{w}_{\boldsymbol{P}} &= \left[\begin{array}{cc} \boldsymbol{\omega}_{\mathcal{B}_{0\times}} & \boldsymbol{0} \\ \boldsymbol{v}_{\boldsymbol{P}_{0\times}} & \boldsymbol{\omega}_{\mathcal{B}_{0\times}} \end{array} \right] \left[\begin{array}{cc} m\boldsymbol{I}_3 & \boldsymbol{S}_{\boldsymbol{P}}^T \\ \boldsymbol{S}_{\boldsymbol{P}} & \boldsymbol{J}_{\boldsymbol{P}} \end{array} \right] \left\{ \begin{array}{c} \Delta\boldsymbol{v}_{\boldsymbol{P}} \\ \Delta\boldsymbol{\omega}_{\mathcal{B}} \end{array} \right\}, \\ \Delta\boldsymbol{w}_{\boldsymbol{P}} \times \boldsymbol{M}_{\boldsymbol{P}}^i \boldsymbol{w}_{\boldsymbol{P}_0} &= \\ -\left(\boldsymbol{M}_{\boldsymbol{P}}^i \boldsymbol{w}_{\boldsymbol{P}_0}\right)_\times \Delta\boldsymbol{w}_{\boldsymbol{P}} &= -\left(\left[\begin{array}{cc} m\boldsymbol{I}_3 & \boldsymbol{S}_{\boldsymbol{P}}^T \\ \boldsymbol{S}_{\boldsymbol{P}} & \boldsymbol{J}_{\boldsymbol{P}} \end{array} \right] \left\{ \begin{array}{c} \boldsymbol{v}_{\boldsymbol{P}_0} \\ \boldsymbol{\omega}_{\mathcal{B}_0} \end{array} \right\}\right)_\times \left\{ \begin{array}{c} \Delta\boldsymbol{v}_{\boldsymbol{P}} \\ \Delta\boldsymbol{\omega}_{\mathcal{B}} \end{array} \right\}.\end{aligned} \tag{27}$$

Both expressions can be normally written by components assuming a body reference, where the fully-populated generalized mass matrix $\boldsymbol{M}_{\boldsymbol{P}}^{i}$ has usually constant components within a maneuver for an airship considered as a rigid body.

2.2.2. Kinematic relations for rotational speed and Euler parameters

Considering the kinematic relations in Eq. (6), their linearization requires replacing all quantities on the l.h.s. and r.h.s. with corresponding linear expansions. By substituting and purging the identity holding in a reference condition, the following perturbation form is obtained

$$\Delta\dot{\boldsymbol{e}}_{321}^{\mathcal{B}} = \boldsymbol{S}_{321_0}^{\mathcal{B}^{-1}}\Delta\boldsymbol{\omega}_{\mathcal{B}}^{\mathcal{B}} + \Delta\boldsymbol{S}_{321}^{\mathcal{B}^{-1}}\boldsymbol{\omega}_{\mathcal{B}_0}^{\mathcal{B}}, \tag{28}$$

The term $\Delta\boldsymbol{S}_{321}^{\mathcal{B}^{-1}}$ can be computed by performing the differential of $\boldsymbol{S}_{321}^{\mathcal{B}^{-1}}$, and is clearly a function of $\Delta\boldsymbol{e}_{321}^{\mathcal{B}}$. Upon substitution in Eq. (28), developing the products and factorizing $\Delta\boldsymbol{\omega}_{\mathcal{B}}^{\mathcal{B}}$ and $\Delta\boldsymbol{e}_{321}^{\mathcal{B}}$, the following expression is obtained,

$$\begin{aligned}
\Delta\dot{\boldsymbol{e}}_{321}^{\mathcal{B}} = \begin{Bmatrix} \Delta\dot{\varphi} \\ \Delta\dot{\vartheta} \\ \Delta\dot{\psi} \end{Bmatrix} &= \boldsymbol{S}_{321_0}^{\mathcal{B}^{-1}}\Delta\boldsymbol{\omega}_{\mathcal{B}}^{\mathcal{B}} + \boldsymbol{P}_{321_0}^{\mathcal{B}}\Delta\boldsymbol{e}_{321}^{\mathcal{B}} \\
&= \begin{bmatrix} 1 & \tan\vartheta_0\sin\varphi_0 & \tan\vartheta_0\cos\varphi_0 \\ 0 & \cos\varphi_0 & -\sin\varphi_0 \\ 0 & \frac{\sin\varphi_0}{\cos\vartheta_0} & \frac{\cos\varphi_0}{\cos\vartheta_0} \end{bmatrix} \begin{Bmatrix} \Delta p \\ \Delta q \\ \Delta r \end{Bmatrix} + \\
&\quad \left[\begin{matrix} \tan\vartheta_0\left(q_0\cos\varphi_0 - r_0\sin\varphi_0\right) \\ -q_0\sin\varphi_0 - r_0\cos\varphi_0 \\ q_0\frac{\cos\varphi_0}{\cos\vartheta_0} - r_0\frac{\sin\varphi_0}{\cos\vartheta_0} \end{matrix} \right. \hookleftarrow \\
&\quad \left. \begin{matrix} \left(\tan^2\vartheta_0 + 1\right)\left(q_0\sin\varphi_0 + r_0\cos\varphi_0\right) & 0 \\ 0 & 0 \\ q_0\frac{\sin\vartheta_0\sin\varphi_0}{\cos^2\vartheta_0} + r_0\frac{\sin\vartheta_0\cos\varphi_0}{\cos^2\vartheta_0} & 0 \end{matrix} \right] \begin{Bmatrix} \Delta\varphi \\ \Delta\vartheta \\ \Delta\psi \end{Bmatrix}.
\end{aligned} \tag{29}$$

Notably, in Eq. (29) a term in $\Delta\boldsymbol{e}_{321}^{\mathcal{B}}$, often unnecessarily purged by specifically deploying hypotheses on the reference condition such to make the corresponding matrix multiplier null [46], has been retained for generality.

2.2.3. Kinematic relations for velocity and ground position

Considering now the kinematic relations in Eq. (7), again a linear expansion for each quantity appearing on both sides of the equation is introduced. Upon substitution, and elimination of the identity yielding in reference conditions, it is possible to obtain the perturbation form

$$\Delta\dot{\boldsymbol{x}}_{\boldsymbol{P}}^{\mathcal{I}} = \boldsymbol{R}_{\mathcal{I}\to\mathcal{B}_0}^{\mathcal{I}}\Delta\boldsymbol{v}_{\boldsymbol{P}}^{\mathcal{B}} + \Delta\boldsymbol{R}_{\mathcal{I}\to\mathcal{B}}^{\mathcal{I}}\boldsymbol{v}_{\boldsymbol{P}_0}^{\mathcal{B}}. \tag{30}$$

An elegant analytic expression of the last term on the r.h.s. of Eq. (30) can be written, by first recalling Poisson's rule, according to which

$$\dot{\boldsymbol{R}}_{\mathcal{I}\to\mathcal{B}}^{\mathcal{I}} = \boldsymbol{\omega}_{\mathcal{B}_\times}^{\mathcal{I}}\boldsymbol{R}_{\mathcal{I}\to\mathcal{B}}^{\mathcal{I}} = \boldsymbol{R}_{\mathcal{I}\to\mathcal{B}}^{\mathcal{I}}\boldsymbol{\omega}_{\mathcal{B}_\times}^{\mathcal{B}} = \boldsymbol{R}_{\mathcal{I}\to\mathcal{B}}^{\mathcal{I}}\left(\boldsymbol{S}_{321}^{\mathcal{B}}\dot{\boldsymbol{e}}_{321}^{\mathcal{B}}\right)_\times. \tag{31}$$

Employing Eq. (31) on the perturbation forms $\Delta\boldsymbol{R}_{\mathcal{I}\to\mathcal{B}}$ and $\Delta\boldsymbol{e}_{321}^{\mathcal{B}}$ (instead of the corresponding rates), it is possible to write the equivalence

$$\Delta\boldsymbol{R}_{\mathcal{I}\to\mathcal{B}}^{\mathcal{I}} = \boldsymbol{R}_{\mathcal{I}\to\mathcal{B}_0}^{\mathcal{I}}\left(\boldsymbol{S}_{321_0}^{\mathcal{B}}\Delta\boldsymbol{e}_{321}^{\mathcal{B}}\right)_\times. \tag{32}$$

By replacing Eq. (32) in the last term of Eq. (30), and elaborating it to factorize $\Delta\boldsymbol{e}_{321}^{\mathcal{B}}$, the following is obtained,

$$\begin{aligned}
\Delta\boldsymbol{R}_{\mathcal{I}\to\mathcal{B}}^{\mathcal{I}}\boldsymbol{v}_{\boldsymbol{P}_0}^{\mathcal{B}} &= \boldsymbol{R}_{\mathcal{I}\to\mathcal{B}_0}^{\mathcal{I}}\left(\boldsymbol{S}_{321_0}^{\mathcal{B}}\Delta\boldsymbol{e}_{321}^{\mathcal{B}}\right)_\times\boldsymbol{v}_{\boldsymbol{P}_0}^{\mathcal{B}} \\
&= -\boldsymbol{R}_{\mathcal{I}\to\mathcal{B}_0}^{\mathcal{I}}\boldsymbol{v}_{\boldsymbol{P}_{0_\times}}^{\mathcal{B}}\left(\boldsymbol{S}_{321_0}^{\mathcal{B}}\Delta\boldsymbol{e}_{321}^{\mathcal{B}}\right) = -\left(\boldsymbol{R}_{\mathcal{I}\to\mathcal{B}_0}^{\mathcal{I}}\boldsymbol{v}_{\boldsymbol{P}_{0_\times}}^{\mathcal{B}}\boldsymbol{S}_{321_0}^{\mathcal{B}}\right)\Delta\boldsymbol{e}_{321}^{\mathcal{B}}.
\end{aligned} \tag{33}$$

Substituting Eq. (33) into Eq. (30) produces a form where the time derivative on the l.h.s., in a similar fashion to Eq. (29), is a function of (in this case) the current perturbed velocity $\Delta\boldsymbol{v}_{\boldsymbol{P}}^{\mathcal{B}}$ and Euler parameters $\Delta\boldsymbol{e}_{321}^{\mathcal{B}}$.

2.2.4. Linearization of the forcing terms in the dynamic balance equations

As stated previously in this section, the perturbed forms of the actions on the r.h.s. of Eq. (26) can be obtained numerically with a finite-difference perturbation method. This process is physically performed by first assigning the reference state of the system s_0, the reference controls δ_0 (where $\delta = \left\{\delta^e, \delta^t\right\}^T$ conveys the aerodynamic controls and thrust controls in a column vector), and the environmental conditions constituted by the density of air ρ, the intensity of gravity g, and the wind intensity and direction $\boldsymbol{v}_{W_0}^{\mathcal{I}}$ in ground components (which is usually more convenient to assign than in body components). All actions are computed in these reference conditions. Then the states are perturbed one by one in both a positive and negative direction, and all actions are computed correspondingly. This produces state and control sensitivity matrices $\boldsymbol{W}_{\boldsymbol{P},s}^{(\cdot)}$ and $\boldsymbol{W}_{\boldsymbol{P},\delta}^{(\cdot)}$, for each of the five generalized forces $\boldsymbol{r}_{\boldsymbol{P}}^{(\cdot)}$ mentioned in Eqs. (1) and (26), with the following structure stemming from Eq. (5),

$$\boldsymbol{W}_{\boldsymbol{P},s}^{(\cdot)} = \begin{Bmatrix} \frac{\partial \boldsymbol{f}^{(\cdot)^{\mathcal{I}}}}{\partial s} \\ \frac{\partial \boldsymbol{m}_{\boldsymbol{P}}^{(\cdot)^{\mathcal{I}}}}{\partial s} \end{Bmatrix}, \boldsymbol{W}_{\boldsymbol{P},\delta}^{(\cdot)} = \begin{Bmatrix} \frac{\partial \boldsymbol{f}^{(\cdot)^{\mathcal{I}}}}{\partial \delta} \\ \frac{\partial \boldsymbol{m}_{\boldsymbol{P}}^{(\cdot)^{\mathcal{I}}}}{\partial \delta} \end{Bmatrix}. \tag{34}$$

Notably, as highlighted in Section 2.1.1 when going through the analysis of each generalized force term one by one, according to the dependencies assumed in this research, not all generalized forces shall depend on all states and controls. This will be numerically reflected by null values in the corresponding positions of the sensitivity matrices. Considering the r.h.s. of Eq. (26), according to Eq. (34), the perturbation form of each of the generalized force terms can be written as

$$\Delta\boldsymbol{r}_{\boldsymbol{P}}^{(\cdot)} = \boldsymbol{W}_{\boldsymbol{P},s}^{(\cdot)}\Delta s + \boldsymbol{W}_{\boldsymbol{P},\delta}^{(\cdot)}\Delta\delta. \tag{35}$$

2.2.5. States-space form of the linearized equations

Based on the development of the linearized forms of all terms just introduced, the complete system of dynamic balance and kinematic equations in linearized form can be written at first as typical to a mechanical system (i.e. with reaction on the l.h.s. and the action on the r.h.s.), yielding

$$\tilde{\boldsymbol{M}}\Delta\dot{s} + \tilde{\boldsymbol{K}}\Delta s = \tilde{\boldsymbol{W}}_{\boldsymbol{P},s}\Delta s + \tilde{\boldsymbol{W}}_{\boldsymbol{P},\delta}\Delta\delta. \tag{36}$$

Correspondingly, in Eq. (36), the 12-by-12 mass and stiffness matrices on the l.h.s. take the form

$$\begin{aligned}
\tilde{\boldsymbol{M}} &= \begin{bmatrix} \left(\boldsymbol{M}_{\boldsymbol{P}}^{i} + \boldsymbol{M}_{\boldsymbol{P}}^{a}\right) & \boldsymbol{0}_6 \\ \boldsymbol{0}_6 & \boldsymbol{I}_6 \end{bmatrix}, \\
\tilde{\boldsymbol{K}} &= \begin{bmatrix} \multicolumn{2}{c}{\left(\left(\boldsymbol{w}_{\boldsymbol{P}_{0_\times}}\boldsymbol{M}_{\boldsymbol{P}}^{i}\right) - \left(\boldsymbol{M}_{\boldsymbol{P}}^{i}\boldsymbol{w}_{\boldsymbol{P}_0}\right)_\times\right)} & \multicolumn{2}{c}{\boldsymbol{0}_6} \\ \boldsymbol{0}_3 & -\boldsymbol{S}_{321_0}^{\mathcal{B}^{-1}} & -\boldsymbol{P}_{321_0}^{\mathcal{B}} & \boldsymbol{0}_3 \\ -\boldsymbol{R}_{\mathcal{I}\to\mathcal{B}_0}^{\mathcal{I}} & \boldsymbol{0}_3 & \left(\boldsymbol{R}_{\mathcal{I}\to\mathcal{B}_0}^{\mathcal{I}}\boldsymbol{v}_{\boldsymbol{P}_{0_\times}}^{\mathcal{B}}\boldsymbol{S}_{321_0}^{\mathcal{B}}\right) & \boldsymbol{0}_3 \end{bmatrix},
\end{aligned} \tag{37}$$

whereas the sensitivity matrices on the r.h.s. of Eq. (36) take the simple form

$$\begin{aligned}
\tilde{\boldsymbol{W}}_{\boldsymbol{P},s} &= \begin{bmatrix} \boldsymbol{W}_{\boldsymbol{P},s}^{a} + \boldsymbol{W}_{\boldsymbol{P},s}^{b} + \boldsymbol{W}_{\boldsymbol{P},s}^{g} + \boldsymbol{W}_{\boldsymbol{P},s}^{p} + \boldsymbol{W}_{\boldsymbol{P},s}^{t} \\ \boldsymbol{0}_{6\times 12} \end{bmatrix}, \\
\tilde{\boldsymbol{W}}_{\boldsymbol{P},\delta} &= \begin{bmatrix} \boldsymbol{W}_{\boldsymbol{P},\delta}^{a} + \boldsymbol{W}_{\boldsymbol{P},\delta}^{b} + \boldsymbol{W}_{\boldsymbol{P},\delta}^{g} + \boldsymbol{W}_{\boldsymbol{P},\delta}^{p} + \boldsymbol{W}_{\boldsymbol{P},\delta}^{t} \\ \boldsymbol{0}_{6\times N_\delta} \end{bmatrix},
\end{aligned} \tag{38}$$

wherein the number of control N_δ is the sum of the number of aerodynamic controls (typically three, representing control settings around the three body axes) and thrust controls (typically the same number as the thrusters on-board, N_T).

From Eqs. (36)–(38), it is immediate to compute the matrices of a states-space representation of the system, respectively the state matrix $\boldsymbol{A}$ and control sensitivity matrix $\boldsymbol{B}$ as

$$\boldsymbol{A} = \tilde{\boldsymbol{M}}^{-1}\left(\tilde{\boldsymbol{W}}_{\boldsymbol{P},s} - \tilde{\boldsymbol{K}}\right), \ \boldsymbol{U} = \tilde{\boldsymbol{M}}^{-1}\tilde{\boldsymbol{W}}_{\boldsymbol{P},\delta}, \tag{39}$$

such that $\Delta\dot{s} = \boldsymbol{A}\Delta s + \boldsymbol{U}\Delta\delta$.

Table 1
Positions of the motors on-board the considered airship.

Motor ID	Position $q_{T_i}^{\mathcal{B}}$ [m]	Positive thrust direction
#1	$\{-9.07, 0, 0\}^T$	Forward
#2	$\{-9.07, 0, 0\}^T$	Downward
#3	$\{2.0, -1.8634, 0\}^T$	Upward
#4	$\{2.0, 1.8634, 0\}^T$	Upward
#5	$\{0, -1.9905, 0\}^T$	Forward
#6	$\{0, 1.9905, 0\}^T$	Forward

Table 2
Geometric and inertial data of the considered airship model.

Sizing data	Value
Mass m [kg]	136.8
Volume $\mathcal{V}$ [m^3]	110.3
Envelope length [m]	16.0
Maximum radius [m]	1.99
Center of buoyancy from origin of body reference $\boldsymbol{q}_{\boldsymbol{B}}^{\mathcal{B}}$ [m]	$\{0, 0, 0\}^T$
Center of gravity from origin of body reference $\boldsymbol{q}_{\boldsymbol{G}}^{\mathcal{B}}$ [m]	$\{-0.06, 0, 0.455\}^T$
Diagonal inertia components $J_{P,1}$, $J_{P,2}$, $J_{P,3}$ [kgm^2]	214, 3,310, 3,211
Non-diagonal inertia components $J_{P,12}$, $J_{P,13}$, $J_{P,23}$ [kgm^2]	0, -88, 0
Munk's factors k_1, k_2, k_3 [kg/m^3], k' [kg]	0.08, 0.86, 0.86, 0.69
Apparent inertia J_2^a, J_3^a [m^2]	13.6, 13.6

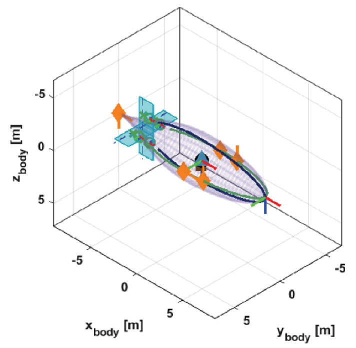

Fig. 5. Topology of the reference airship in SILCROAD. Orange diamonds: Position of thrusters (Orange arrow: Nominal direction of corresponding thrust). Blue triangle: Center of buoyancy. Black square: Center of gravity. (For interpretation of the references to color in this figure legend, the reader is referred to the web version of this article.)

3. Free response of a tethered airship in static equilibrium

This and the next section (see Section 4) serve the double aim of investigating the characteristics of the docking maneuver for a realistic airship, and displaying the ability of the mid-fidelity model introduced in Section 2 for the airship and tether cables to produce interesting results, sensitive to changes in many parameters relevant to the design of the airship and the testing scenario.

To the aim of investigating the free response of the system, a practical testing scenario has been introduced. An ideal airship with the same envelope and tail empennages of the experimental *Lotte* machine [20,26] has been considered. Notably, such envelope is axial-symmetric, featuring a simple cruciform tail and a single motor in the tail cone. However, unlike the real machine, the investigated model is not controlled by means of any aerodynamic controls (i.e., figuratively the deflection of the rudder and elevons is permanently set to a null value). Instead, $N_T = 6$ electric motors have been considered in the airship concept at hand, positioned as reported in Table 1 with respect to a body reference centered in the center of buoyancy $\boldsymbol{B}$.

In essence, motors #1 and #2 are positioned to the back of the airship (tail cone), with #1 longitudinally aligned (similar to the original configuration of the *Lotte*) and #2 aligned with the positive direction of the body reference unit vector $\boldsymbol{b}_3$ (i.e. downwards). Motor #3 and #4 are positioned symmetrically, respectively to the port and to the starboard sides of the airship, 2 m forward with respect to the longitudinal position of the center of buoyancy $\boldsymbol{B}$, on the horizontal plane of symmetry of the envelope, and they point upwards. Finally, #5 and #6 are again symmetrically located respectively to the port and to the starboard sides of the airship, longitudinally at the level of point $\boldsymbol{B}$ and on the horizontal plane of symmetry of the envelope, and pointing forward. Additional basic data are reported in Table 2.

In a baseline configuration, a single cable has been considered, with a nominal length $L_{t_1} = 20$ m. The technological characteristics refer to a common polyester braided rope for nautical applications, with a diameter $D_t = 10$ mm and a linear density $\rho_t = 80$ g/m, yielding a breaking tension of $F_b = 3{,}040$ N [48]. The value of the stiffness of the stretched cable has been estimated based on a regression of catalog data [49,50], yielding $K_0 = 6.976 \cdot 10^4$ N. The limit elongation values for the three different tension models (see paragraph Section 2.1.2) have been set to $e_{i,c} = 0.99$ and $e_{i,e} = 1.05$ respectively. The ground anchor point $\boldsymbol{AP}_1$ has been set at the origin of the ground reference, yielding $\boldsymbol{AP}_1^{\mathcal{I}} = \{0, 0, 0\}^T$, whereas in the baseline configuration the position of the tether point $\boldsymbol{TP}_1$ is assumed at the nose tip of the airship, i.e. $q_{\boldsymbol{TP}_1}^{\mathcal{B}} = \{6.97, 0, 0\}^T$ m. The reference measuring point $\boldsymbol{P}$ has been set at the center of buoyancy $\boldsymbol{B}$, as can be seen from Table 2 (note $\boldsymbol{q}_{\boldsymbol{B}}^{\mathcal{B}}$ is null correspondingly).

A non-linear model for tethered airship dynamics has been set up employing the SILCROAD library [5,17,51], which implements the formulation described in Section 2.1. The topology of the reference airship as specified in SILCROAD is shown in Fig. 5.

The library has been suitably expanded in this research, allowing the user to include an unlimited number of tethering cables, each treated as a separate object obtained as the instantiation of a newly designed class. The latter implements the model described in Section 2.1.2. The non-linear model of the tethered airship has been employed first to solve a non-linear trim problem, finding a static equilibrium condition represented by a state $\boldsymbol{s}_0$ and a control array $\boldsymbol{\delta}_0 = \boldsymbol{\delta}_0^t$. In that problem, the airship is automatically trimmed by means of thrust controls, so as to guarantee $\dot{\boldsymbol{s}} = \boldsymbol{0}$, while keeping null values of the velocity and rotational rate ($\boldsymbol{v}_{\boldsymbol{P},0}^{\mathcal{B}} = \boldsymbol{0}$ and $\boldsymbol{\omega}_{\mathcal{B},0}^{\mathcal{B}} = \boldsymbol{0}$), a neutral attitude ($\boldsymbol{e}_{321_0}^{\mathcal{B}} = \boldsymbol{0}$) and a specific position of the tether point $\boldsymbol{TP}_1^{\mathcal{I}}$ in space, specified by components in the ground reference $\mathcal{I}$, such to produce an assigned reference elongation ratio $e_{1_0} = 0.8$. Additionally, in the trimmed condition the airship (including its tethering system) is subject to a uniform horizontal reference wind $\boldsymbol{v}_{W,0}$, assigned in ground components, such to blow from North to South. The airship is trimmed so that the wind vector lye in the vertical plane of symmetry ($\psi = 0$, as said). The selection of this specific trimmed condition is consistent with the analysis of the controlled response in a dynamic docking maneuver of interest in this research, for which this static equilibrium condition constitutes an initial condition. Figuratively, the machine is thus trimmed in a tethered condition, where the cable has been unwound from the airship tether point and linked to the anchoring point, in a non-idling thrust condition from where the airship can start a controlled docking maneuver.

It should be observed that the trim problem just specified is radically different from that of a tethered aerostat, in that an aerostat cannot keep a generic reference condition in space, but the latter is determined by the characteristics of the tether cable (in particular, its length and positioning of the tether point on board), the intensity of the wind and the aerostatic, aerodynamic and inertial characteristics (in particular, the positioning of the center of gravity vs. the center of buoyancy and tether point/s) of the aerostat.

For studying the free response, linearization is performed according to the method explained in Section 2.2 (implemented in the routines of the SILCROAD library). The study of the free response can be carried out by computing the eigenvalues and eigenvectors of the state matrix $\boldsymbol{A}$ corresponding to a certain state $\boldsymbol{s}_0$, wind $\boldsymbol{v}_{W,0}$ and control $\boldsymbol{\delta}_0$ (computed such to satisfy static equilibrium, i.e. trim). In the following, as stated in the introduction (Section 1), the effect of the presence and of the

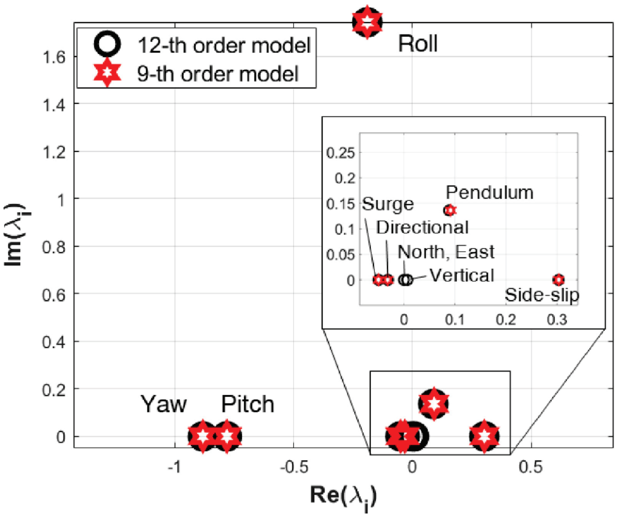

Fig. 6. Eigenvalues of the untethered airship trimmed in fixed-point conditions in an opposing wind of 6 m/s, as described in the text. Comparison of eigenvalues pertaining to a 9th order model, typically employed for airship flight dynamics, and a 12th order model, required for tethered flight analysis.

characteristics of the tether cable and of the trim problem setting will be shown in a parameterized fashion.

3.1. Effect of a tether cable on the free response

A typical eigenanalysis of the free response of an untethered airships is carried out on a reduced state, where in particular the three positional states $\boldsymbol{x}_{\boldsymbol{P}}^{\mathcal{I}}$ are not considered. Correspondingly, nine eigenvalues are featured in the eigendynamics of the system, where the fastest are the real, typically largely stable eigenvalues corresponding to pitch and yaw subsidence modes, the slowest are the real ones associated to longitudinal surge, typically stable, and the generally unstable side-slip subsidence. Two couples of complex conjugate eigenvalues are associated respectively to pendulum mode, which might be mildly stable or unstable, and the high-frequency, typically stable roll oscillation. Finally a null mode mostly associated to yaw (ψ) is in order for an airship moving in calm air (no wind), replaced by a real, low frequency directional mode when the airship is traveling in a wind stream. Fig. 6 displays the eigenmodes just mentioned for the reference airship, standing in static equilibrium and still with respect to the ground reference (i.e., $\boldsymbol{v}_{\boldsymbol{P}} = \boldsymbol{0}$, $\boldsymbol{\omega}_{\mathcal{B}} = \boldsymbol{0}$) while untethered, pointing North, and immersed in an opposing uniform wind stream $\boldsymbol{v}_{W,0}$ of intensity 6 m/s (blowing to the South). Furthermore, the attitude angles $\boldsymbol{e}^{\mathcal{B}}_{321_0} = \boldsymbol{0}$. In this condition, no null mode can be found in the reduced-order (i.e., 9th order) dynamics of the system. However, when introducing the additional three states corresponding to $\boldsymbol{x}_{\boldsymbol{P}}^{\mathcal{I}}$ (in particular, with the position of the buoyancy center $\boldsymbol{B}$ such that $\boldsymbol{x}^{\mathcal{I}}_{\boldsymbol{TP}_1} = e_{1_0} L_t\{-\cos(\pi/4), 0, -\sin(\pi/4)\}^T$), three additional eigenvalues are obtained.

Of these, two correspond to horizontal translation (North, East), whereas the latter to vertical translation. The former two are associated to zero frequency, since there is no difference in trimming the (untethered) airship at whatever couple of horizontal geographical coordinates, whereas the latter is non-zero, and mildly unstable, since there is a slight difference on buoyancy and aerodynamic forces in changing the altitude, due to the effect of density (a function of the altitude according to the International Standard Atmosphere model implemented in SILCROAD).

For a better understanding the impact of a tether force, it is interesting at first to study how these eigenvalues evolve when adding to the scenario an ideal tethering cable, featuring at first very light density and small diameter, and progressively featuring an increasing value of both quantities. For a negligible diameter and density, the tension at $\boldsymbol{TP}_1$ shall be negligible, impacting the results of the eigenanalysis only minimally. Conversely, for increasing values of the cable-specific parameters, corresponding to cables realistically employed in practice, a difference is noted in the results of the eigenanalysis. The tether is anchored as previously specified, with the tether point $\boldsymbol{TP}_1$ on the nose of the airship, and the airship is in an a position with respect to the ground reference such that $\boldsymbol{TP}_1$ is exactly where it was in the untethered trimmed condition. Taken together, the two plots in Fig. 7 show the change in the map of eigenvalues, as just explained. Both plots are zoomed on the portion pertaining to the slowest eigenmodes (i.e. smallest modulus of the eigenvalues). Actually, with respect to the untethered condition, also the eigenvalues pertaining to higher-frequency modes (namely yaw, pitch, side-slip, as well as roll- and pendulum-oscillation, all visible on Fig. 6) shall change slightly, yet qualitatively keeping very close to their respective untethered values. Conversely, the change of the low-frequency eigenvalues corresponding to surge and directional modes, as well as the newly added North, East and vertical translation modes, is more dramatic, and requires some explanation. Specifically, in the left plot the results of eigenanalysis for an untethered condition are displayed (black circles), representing a theoretical starting point for a tethered analysis where the cable is infinitely thin and infinitesimally heavy. The plot shows the eigenvalues for increasing ρ_t and D_t up to a realistic (albeit weak, for the application at hand), $\rho_t = 6$ g/m and $D_t = 2.5$ mm (blue star). The arrows indicate the identity and evolution of the eigenvalues. It can be observed in particular that the surge mode, with an eigenvector mostly associated to U (first component of $\boldsymbol{v}_{\boldsymbol{B}}^{\mathcal{B}}$) and the northerly component of $x_{\boldsymbol{P}}^{\mathcal{I}}$, tends decidedly towards instability. Also interesting is the fact that one of the two modes identified as null in Fig. 6, associated to a northerly motion (first component of $\boldsymbol{x}_{\boldsymbol{P}}^{\mathcal{I}}$), tends in a similarly decided way towards stability. Additionally, the remaining originally null mode, associated to an Eastern translation (second component of $\boldsymbol{x}_{\boldsymbol{P}}^{\mathcal{I}}$) tends slowly towards a (very slow) instability. Finally, the rightmost among the considered modes, associated to the vertical position (third component of $\boldsymbol{x}_{\boldsymbol{P}}^{\mathcal{I}}$) starts shifting slightly towards stability.

Moving on to the right plot in Fig. 7, this completes the analysis for even increasing values of ρ_t and D_t. The starting condition is the same as the last on the previous plot (blue star), and the analysis considers a maximum value of $\rho_t = 140$ g/m and $D_t = 14$ mm. The red star represents the baseline value of the cable-specific properties, previously mentioned and employed later in this research. In this second plot, it can be seen how, for a heavier/thicker cable, the eigenvalues corresponding to surge and northerly translation coalesce to produce a low-frequency oscillatory mode, which is stable, but with a damping which is progressively reduced as ρ_t and D_t are raised. The other three eigenvalues keep on the real axis. The directional motion and notably the vertical translational mode become increasingly stable, whereas the easterly translational mode turns progressively more unstable.

It is interesting to show how an alternative layout of the cables would impact the results of the eigenanalysis. To this aim, a case where two independent cables are anchored to the sides of the airship is considered. To allow for a fair comparison with respect to the previous solution, the cable-specific physical characteristics have been selected according to the same listing employed for the single cable case. Furthermore, the positioning of the two cables with respect to the ground and to the wind has been assigned so that each of the two cables takes exactly the same shape and carries the same tension load as in the previous case. In particular, the two cables have been attached to tether points 3.77 m towards the nose from point $\boldsymbol{B}$ (a longitudinal station employed also later in the next analyses), on the envelope and on the horizontal plane of symmetry of the airship. The corresponding positions are therefore $\boldsymbol{q}^{\mathcal{B}}_{\boldsymbol{TP}_1} = \{3.77, -1.5977, 0\}^T$ and $\boldsymbol{q}^{\mathcal{B}}_{\boldsymbol{TP}_2} = \{3.77, 1.5977, 0\}^T$. The anchor

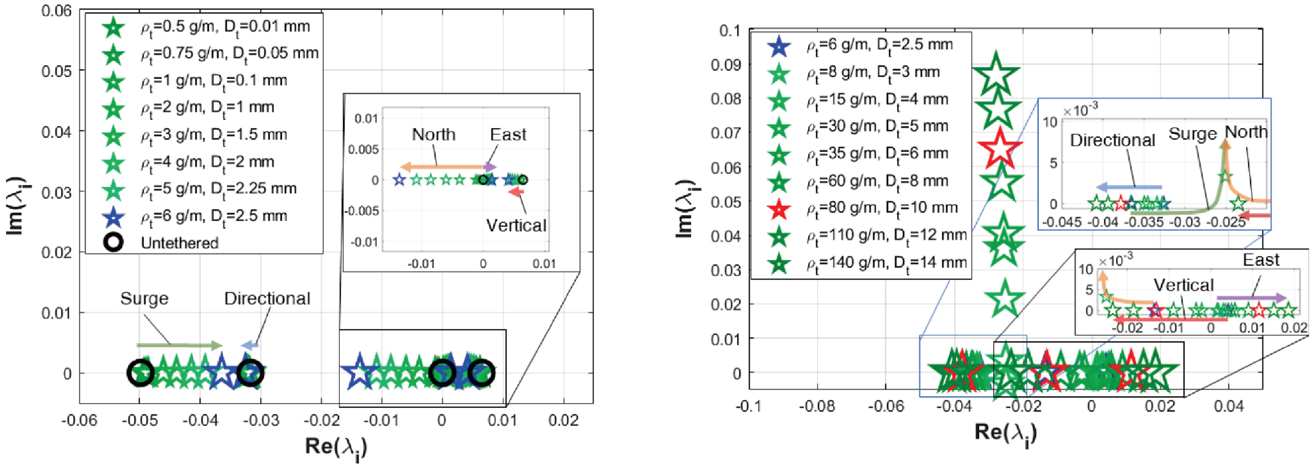

Fig. 7. Eigenvalues of the tethered airship trimmed in fixed-point conditions in an opposing wind of 6 m/s, for increasing density ρ_t and diameter D_t of the cable. Left: Lighter/thinner cable properties. Right: Heavier/thicker cable properties. Blue star: Merging point between plots. Red star: Reference value of cable properties. Black circles: Eigenvalues of untethered system. (For interpretation of the references to color in this figure legend, the reader is referred to the web version of this article.)

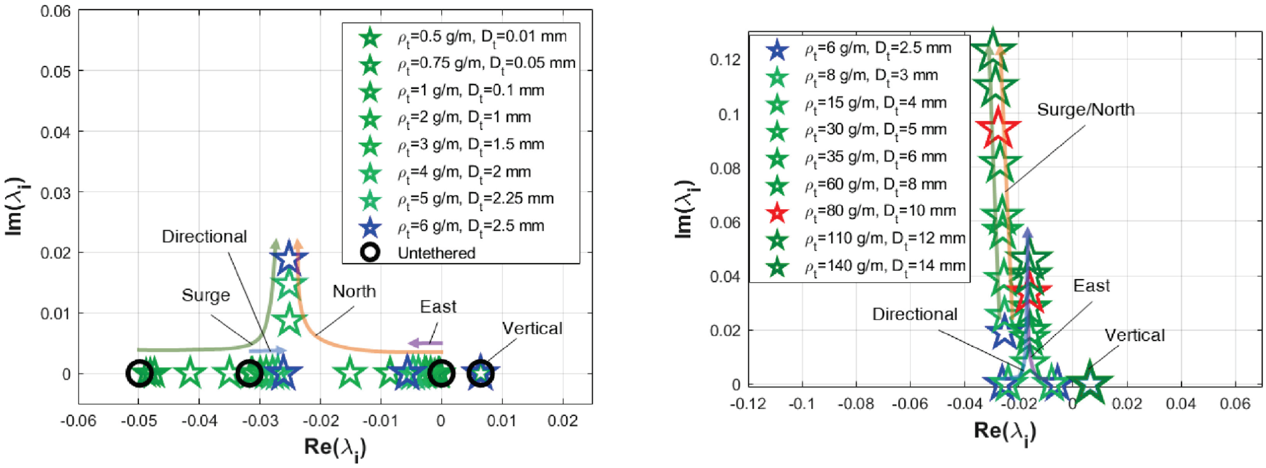

Fig. 8. Eigenvalues of the airship trimmed with two tether cables symmetrically located to the sides, in fixed-point conditions in an opposing wind of 6 m/s, for increasing density ρ_t and diameter D_t of the cable. Left: Lighter/thinner cable properties. Right: Heavier/thicker cable properties. Blue star: Merging point between plots. Red star: Reference value of cable properties. Black circles: Eigenvalues of untethered system. (For interpretation of the references to color in this figure legend, the reader is referred to the web version of this article.)

points on ground are correspondingly specified as $\boldsymbol{x}^{I}_{AP_1} = \{0, -1.5977, 0\}$ and $\boldsymbol{x}^{I}_{AP_2} = \{0, 1.5977, 0\}$, so that the elongation of both cables is $e_{1_0} = e_{2_0} = 0.8$.

The result of the eigenanalysis is displayed in Fig. 8, split in the same way as Fig. 7 for convenience. Again, the focus is on the low-frequency modes (i.e., low-modulus eigenvalues), whereas the quality of others (not visible in the figure) remains qualitatively similar for changing values of the cable-specific parameters.

From the left plot, for a thinner/lighter cable, a different behavior from the single-cable case (Fig. 7 left) is immediately apparent. The longitudinal modes of surge and northerly translation travel faster towards coalescence, giving way to a stable oscillatory motion for lower values of ρ_t and D_t than in the previous case. This can be the effect of the presence of two cables, adding twice the overall tension in the longitudinal domain with respect to a single-cable case. However, a radically different behavior is encountered from the directional and easterly translation modes, which travel respectively towards instability and towards stability (exactly the opposite of the previous case), while keeping real. For increasingly heavier/thicker cables (right plot) the latter eigenvalues coalesce to create an additional oscillatory mode, with an eigenvector polarized on easterly translation and body side velocity (i.e., component V of ground velocity $\boldsymbol{v}^{B}_{B}$). This low-frequency mode is stable, yet it features a reduced level of stability for increased values of the density and diameter of the cables. Generally, this behavior is in line with intuition, showing that two forward-positioned tethering cables, with a symmetric sideward displacement of their tether points with respect to the plane of symmetry (and the wind direction), instead of a single cable attached to the nose, make the airship more stable in terms of cross-wind (i.e., easterly) ground position, while on the other hand activating an oscillatory response in the lateral directional plane. Notably, the mode associated primarily to vertical translation (i.e., normal to the horizon) does not feature a significant travel in this case. This may be the result of the longitudinal positioning of the tether points closer to the center of buoyancy and center of mass with respect to the single-cable case, inducing a less relevant action of tension in the balance equation around the pitch axis along $\boldsymbol{b}_2$ (more on the effect of longitudinal positioning of the tether point in the next Section 3.2).

3.2. Effect of longitudinal positioning of the tether point

Referring again to the original reference condition mentioned in the previous example (see Section 3.1, single cable with assigned reference

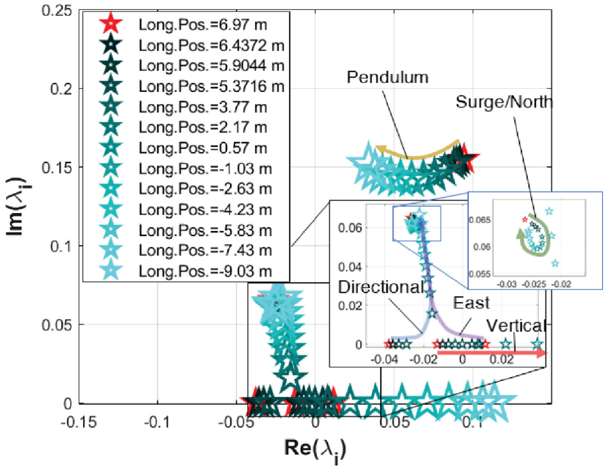

Fig. 9. Eigenvalues of the tethered airship trimmed in fixed-point conditions in an opposing wind of 6 m/s, for positions of the tether attachment point shifting from the nose to the tail. Red star: Reference value of tether point position on-board. (For interpretation of the references to color in this figure legend, the reader is referred to the web version of this article.)

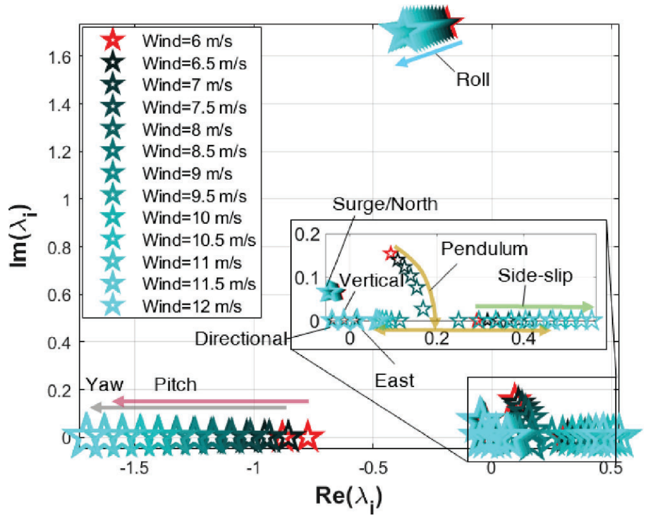

Fig. 10. Eigenvalues of the tethered airship trimmed in fixed-point conditions in an opposing wind of increasing intensity between 6 and 12 m/s. Red star: Reference value of the wind speed. (For interpretation of the references to color in this figure legend, the reader is referred to the web version of this article.)

properties), represented by the red star in Fig. 7, it is possible to analyze the effect of a change of the longitudinal position of the on-board tether point $\boldsymbol{TP}_1$. In this case, the analysis has been parameterized so that the cable solution be exactly the same for all cases, by keeping the position of the tether point in ground coordinates $\boldsymbol{TP}_1^{\mathcal{I}}$ the same in all cases, and by suitably changing the position of the airship to cope with a different position $\boldsymbol{q}_{\boldsymbol{TP}_1}$ of the anchor point $\boldsymbol{TP}_1^{\mathcal{B}}$ with respect to the airship layout. The position of the on-board tether point has been selected to be on the bottom chin line along the airship surface, on the external surface of the latter. Longitudinal positions have been considered ranging from the nose (reference condition) to the tail. A finer discretization has been considered in proximity to the nose. The plot in Fig. 9 shows the eigenvalues resulting for each considered position, zooming on the low-frequency area (non visible are yaw, pitch, side-slip and roll oscillation).

Besides a relevant change in the real part of pendulum (which remains unstable), and an instability of the eigenvalue associated to a mainly vertical motion (i.e., with the eigenvector associated mostly to the third component of $\boldsymbol{x}_{\boldsymbol{B}}^{\mathcal{I}}$ normal to the horizon), the most significant result in terms of quality of the response is the coalescence of the eigenvalues associated to directional stiffness and to the easterly-oriented translation (i.e., the second component of $\boldsymbol{x}_{\boldsymbol{B}}^{\mathcal{I}}$). As it can be observed, for a longitudinal position of the tether point between 5.37 m and 3.77 m from $\boldsymbol{B}$, these two modes merge into a new lateral-directional oscillatory mode, featuring an increasing frequency and a reduced damping (yet keeping stable) as the position of the tether point shifts backwards. This is in line with intuition, since the positioning of the anchor point to the back of the airship, in a generic laterally-perturbed condition (e.g., a perturbation in yaw), would tend to pull the tail forward, inducing a rotation around the yawing axis, and triggering a sideward motion. Notably, also the surge/north longitudinal mode is interested by a change, which however does not alter its quality significantly.

3.3. Effect of wind intensity

An interesting effect in presence of a tether cable is observed when increasing the intensity of the wind. In Fig. 10 is reported the map of the airship eigenvalues for a wind intensity between 6 and 12 m/s (notably, the latter is the top speed in the performance envelope of *Lotte*). An appreciable stabilizing effect is immediately visible on pitch and yaw, similar to what happens for a faster-traveling untethered airship. The comparison with the untethered airship holds also for the cases of roll and side-slip modes. Conversely, the pendulum is influenced in a completely different way than in the tethered case. As known, this mode is generally turned slightly towards instability by an increased traveling speed, keeping roughly the same frequency, and becoming insensitive to speed for higher values of this parameter, for an untethered airship. Conversely, pendulum is here affected more markedly for increasing values of the wind speed, with a stark increase in damping, which produces the break-down of the mode into two real modes, which for extreme values of the airspeed travel towards stability and instability, respectively. This effect is bound to the action of the tension, which increases dramatically with the wind speed. By acting on the nose as in this case, it is capable of altering the pitch equilibrium balance. Qualitatively, it is an additional force acting in a similar way as weight (similar direction, intensity increasing with the wind speed), yet displaced forward in its line of action with respect to the other force centers ($\boldsymbol{G}$ and $\boldsymbol{B}$). The balance of buoyancy- and weight-induced moment which produces pendulum is therefore altered by the addition of a progressively prevailing downward force. For a sufficiently intense wind, when perturbed from equilibrium, the airship tends to slowly diverge (longitudinally capsizing) as returned by the two real eigenvalues, associated mostly to pitch and vertical velocity.

3.4. Effect of tether cable elongation

Another relevant parameterization is that with respect to cable elongation. Considering again the baseline configuration described in the introduction to this section, and a wind intensity of 6 m/s, trimmed solutions have been obtained for changing values of the elongation parameter e_{1_0} of the cable. To this aim, the length of the cable L_{t_1} has been left to its nominal value (20 m), and the position $\boldsymbol{x}_{\boldsymbol{B}}$ of the airship in space has been changed to obtain the desired elongation, so that the tether point position be $\boldsymbol{x}_{\boldsymbol{TP}_1}^{\mathcal{I}} = e_{1_0} L_t \{-\cos(\pi/4), 0, -\sin(\pi/4)\}^T$. Values of the elongation between 0.5 and 0.95 have been considered.

The results are displayed in Fig. 11.

Looking at the lower frequency modes in the zoomed plot, a progressive increase in the frequency and decrease in the damping of longitudinal pendulum, as well as of the coalesced modes of surge and northerly motion, can be observed for increasing values of cable elongation. Of special interest are the three last points in the analysis, which reach very close to the domain where the elastic reaction of the cable is assumed relevant and is added to the computation (see Eq. (13)). Where the global behavior of the frequencies is relatively little changed for an

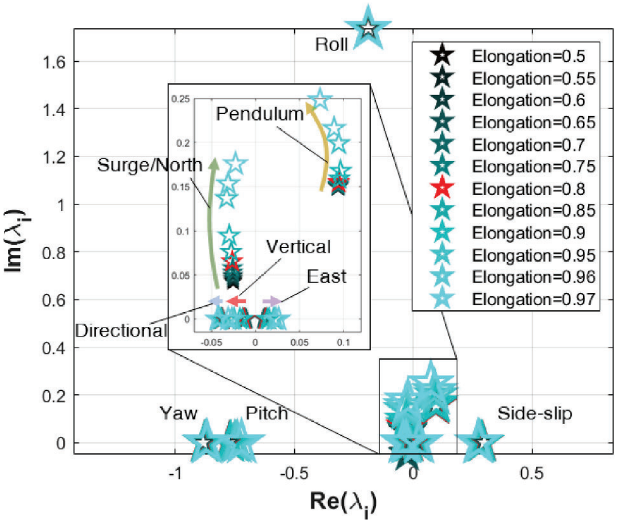

Fig. 11. Eigenvalues of the tethered airship trimmed in fixed-point conditions, for different values of the elongation parameter e_{1_0} in an opposing wind of 6 m/s. Red star: Reference value of the elongation of the tether cable. (For interpretation of the references to color in this figure legend, the reader is referred to the web version of this article.)

elongation up to $e_{1_0} = 0.9$, over this value a much greater sensitivity to elongation can be noticed (note that the last three points are set at a finer discretization, compared to the other in the considered range). This shows that for an increased stretch the response of the system starts to change at an increased pace. This is expected, since for a fully-stretched cable the very stiff elastic reaction shall change the map of eigenvalues substantially. It can be reported that the trimmability of the airship under elongation conditions over those considered here is increasingly problematic, since the thrust required from some of the thrusters for keeping the airship in a stand-still position comes close or exceeds the corresponding nominal thrust, to the point that attaining static equilibrium turnes de facto impossible. Therefore, the application of linear analysis to the corresponding cases would be of limited practical value.

4. Response of a tethered airship in a dynamic docking maneuver

In this section, the non-linear model introduced in Section 2 is employed to analyze the behavior of the airship through dynamic simulations. In particular, the tethered docking phase faced by a small-scale machine is considered. Simple controllers are applied and compared. These analyses do not have the ambition of defining a best-practice for control in a tethered docking maneuver, yet they show two relevant effects. Firstly, the simulation model at hand allows for a sufficient resolution to test differences in performance between control laws, thus showing its suitability for control design and testing applications, possibly of interest for certification-compliant design. Secondarily, they indeed witness that, despite their simplicity, the proposed control laws allow to effectively control a small unmanned airship in a challenging docking scenario, also highlighting the progress in performance obtained through additional control layers.

Through the analysis of the free response of a tethered airship in the vicinity of an equilibrium condition, shown in the previous Section 3, ideally representing the starting point of a docking maneuver, it is possible to note that the inherent behavior of the airship, where different from that of a free airship traveling forward in a calm air condition (i.e., no wind), is still featuring a sub-set of the same distinctive modes of the airship in free flight, i.e. yaw, pitch, side-slip, as well as pendulum- and roll-oscillation. In addition, a set of three more eigenvalues can be found, introduced by the increased order of the system (in turns, induced by the additional ground-positional states). In particular, it has been shown how the original real eigenvalues pertaining to surge and heading (null) mode combine with these additional three eigenvalues, creating either subsiding or oscillatory dynamics, depending on the setting of the parameters (either cable-specific or scenario-specific). However, it can be noted that the additional modes in the tethered scenario are generally associated to low frequencies, posing mild skill requirements on a human pilot, provided a sufficient control authority has been included in the airship layout at a design level. Concerning the latter, as pointed out in the formulation, in this research the focus is on a purely thrust-controlled machine, a paradigm inspired by the aim of project IPROP [52], and already investigated in consolidated literature by the authors [4,5]. As shown in Fig. 5 and Table 1, the layout of the airship thrusters allows for an effective direct control around the pitch axis ($\boldsymbol{b}_2$, with thrusters #2, #3, #4), roll axis ($\boldsymbol{b}_1$, with thrusters #3, #4) and yaw axis ($\boldsymbol{b}_3$, with thrusters #5, #6), whereas forward thrusting action (along $\boldsymbol{b}_1$) is guaranteed primarily by #1.

Despite the non-critically unstable behavior of the machine, as shown in the cited literature [4,5] and in the linear analyses presented in Section 3, a simple stability augmentation system (SAS) around the three body axes can be employed for increased ease of piloting in the navigation phase. This operates with proportional laws on the yaw and roll rates, and with a proportional-integral law on the pitch rate, feeding-back these measures to selected thrusters to dampen the rotational rates.

In this research, the navigation SAS is replaced by a similar concept, which is more tailored to the need of not just increasing the damping in the rotational free response but also favor the keeping of a neutral attitude around the roll and pitch axes, or analytically setting the target values $\bar{\vartheta} = \bar{\varphi} = 0$ deg. Making use of a reading of the attitude angles, typically obtained in practice from an on-board electronic IMU, it is possible to implement the following SAS/neutral attitude laws (all gains are positive, see Appendix),

$$
\begin{aligned}
\Delta\delta_{T_2}^{SAS} &= -\kappa_q^{SAS} q - \kappa_\vartheta(\vartheta - \bar{\vartheta}),\\
\Delta\delta_{T_3}^{SAS} &= -\kappa_p^{SAS} p - \kappa_\varphi(\varphi - \bar{\varphi}) - \frac{1}{2}\frac{q_{T_{2_1}}^B}{q_{T_{3_1}}^B}(\kappa_q^{SAS} q + \kappa_\vartheta(\vartheta - \bar{\vartheta})),\\
\Delta\delta_{T_4}^{SAS} &= +\kappa_p^{SAS} p + \kappa_\varphi(\varphi - \bar{\varphi}) - \frac{1}{2}\frac{q_{T_{2_1}}^B}{q_{T_{4_1}}^B}(\kappa_q^{SAS} q + \kappa_\vartheta(\vartheta - \bar{\vartheta})),\\
\Delta\delta_{T_5}^{SAS} &= -\kappa_r^{SAS} r,\\
\Delta\delta_{T_6}^{SAS} &= +\kappa_r^{SAS} r.
\end{aligned}
\tag{40}
$$

In Eq. (40), the side thrusters #3, #4 are employed both for roll control and for pitch control, together with #2. Concerning the latter, the ratio of the forward positions of the thrusters (i.e., $q_{T_{2_1}}^B$, $q_{T_{3_1}}^B$ and $q_{T_{4_1}}^B$) are employed to obtain two equal opposing components of the pitching moment in the center of buoyancy $\boldsymbol{B}$ from the combined action of motors #2, #3 and #4. Notably, no control is implemented on ψ, since pointing a prescribed constant heading is not generally interesting in the docking maneuver (more relevant is keeping the airship pointed towards the target, more on this point later).

Docking can be performed in principle by simply rewinding the tether cable. However, the target of automated docking is not just that of taking the airship to a prescribed resting position, but also to avoid reaching excessive values of the cable tension, which may lead to envelope tear and cable failure, as well as to reduce the time for the docking maneuver. Concerning loads, taking inspiration from the original envelope of the *Lotte*, made of PVC, a tether point patch similar in shape to that considered in project IPROP has been considered. This is made of the same fabric as the envelope, soldered and centrally glued to it. Assuming a thickness of 0.45 mm for the envelope and patch and a circular patch with a diameter of 10 cm, from the properties of woven PVC a tear breaking force $F_{bt,env} = 481$ N and a tensile breaking force of $F_{b,env} = 2{,}354$ N have been assumed [53]. These are likely conservative (i.e., low) values, since the area of the tether point is generally much reinforced to allow for a better stress distribution over the surrounding area and a lower local strain. They are mostly employed here to monitor and rank the performance of the controllers. Concerning the winch, it is advisable to match the breaking limit of the cable, i.e. $F_b = 3{,}040$ N for the tether cable introduced as a reference in the previous Section 3. A compatible winch is the South Pacific 900E [54], which can be employed up to a tension of 3,139 N. This electric winch, rated at 1,1 kW (max.) power, allows for a maximum rewind speed of 30 m/min.

In view of a desirable increasing degree of automatization of the docking maneuver, the present paper considers three controllers of increased complexity, described in the next paragraphs.

4.1. Tether rewind control

The simplest rewind controller considered here just acts on the cable rewind rate as a control variable, feeding-back the tension measured on the cable at the tether point $\boldsymbol{TP}_1$, typically available through a dedicated dynamometer. Given the default target rewind rate $\bar{\Psi}$ and a tension threshold F_i', the rewind rate of the cable Ψ is set according to the following law (gain κ_Ψ positive, see Appendix),

$$\Psi = \begin{cases} \max\left(\bar{\Psi} - \kappa_\Psi(|\boldsymbol{F}_i| - F_i'), \Psi_{\min}\right), & |\boldsymbol{F}_i| > F_i' \\ \bar{\Psi}, & |\boldsymbol{F}_i| \le F_i' \end{cases}. \tag{41}$$

In this control, the threshold F_i' is selected to activate a reduction of the default rewind rate when the actual tension modulus $|\boldsymbol{F}_i|$ raises above that value. Such reduction shall be at most down to a boundary value $\Psi_{\min}$, in order not to halt the rewind or even unwind the cable, which would potentially lead to an indefinitely long docking maneuver. In the results presented here, the parameters have been set to $\bar{\Psi} = 0.3$ m/s (equal to 18 m/min), $\Psi_{\min} = 0.01$ m/s (which is compatible with the selected winch), and the tension limit to $F_i' = 144.3$ N, which amounts to $\frac{1}{3}F_{bt,env}$. The gain $\kappa_\Psi = 5{\cdot}10^{-3}$ (m/s)/N, a value tuned by trial and error such to reduce maximum tension over time.

To test this control scheme, as well as those introduced in the next paragraphs, the airship has been firstly trimmed in the same scenario employed for linear analysis (see introduction to Section 3). The reference layout with a single cable attached to the nose has been employed. The elongation for trim is $e_{1_0} = 0.8$. The airship is immersed in a uniform horizontal wind flow, blowing from North to South. Three intensities have been considered, of 6, 9, 12 m/s (where the latter is the limit velocity of the *Lotte* airship). Following trimming, the non-linear model of the airship is integrated over time, starting from a perturbed initial condition where all three Euler parameters $\boldsymbol{e}^{\mathcal{B}}_{321} = \{\varphi, \vartheta, \psi\}$ have been augmented by 10 deg with respect to the null reference $\boldsymbol{e}^{\mathcal{B}}_{321_0} = \boldsymbol{0}$ employed for trim. Over time, a side gust from West to East (i.e., attacking the airship from the port side), modeled as a cosine wave with an intensity equal to $\frac{1}{3}$ of the wind intensity and a period of 5 s, intervenes at $t = 20$ s, injecting a non-negligible time-varying disturbance. The simulation is stopped upon reaching a residual tether length of 1.5 m. Integration is carried out employing a variable-step, variable-order (VSVO) integration algorithm with an order between 1 and 5, suited for stiff differential problems, with a maximum discretization time of 0.025 s. Fig. 12 displays the trajectory, and snapshots of the airship and tether cable every 4 s, from North (top-left), East (top-right) and from top (bottom-right). On the bottom-left plot are displayed the tether length, tension modulus at the tether point $\boldsymbol{TP}_1$ and rewind rate Ψ over time. Together with the tether length, the norm of the position of the tether point $\|\boldsymbol{x}_{\boldsymbol{TP}_1}\|$ is also displayed, allowing the reader to immediately check the elongation of the cable. Dots along the line correspond to the snapshots in the trajectory plots.

As can be seen, the controller is globally incapable of satisfactorily control the tension. Despite a reduction of the rewind rate is triggered by the controller in several occasions, as a result of peak tension values, the tension exceeds the envelope tear breaking limit and reaches the assumed tensile breaking value in one occasion (coming close to the cable breaking tension). Table 3 displays synthetic results for the three considered wind/gust intensities, in terms of maximum and average tension, minimum rewind rate Ψ, time Δt spent above F_b', $F_{bt,env}$, $F_{b,env}$ and F_b, and total time for docking.

From the analysis of the table, it is apparent that the system is not capable of avoiding excessive peaks of the tension in the considered scenario, suggesting its usability only for the lowest wind intensities. Notably, the conditions of peak tension are recorded when the elongation of the cable approaches unity coming from a condition of lower elongation (i.e. from a *sagging* condition of the tether to a more stretched one). Looking at the dynamic behavior of the airship, a very intense sideward motion is experienced as a result of the initial condition, due to the combined action of the wind and the tension of the fully-stretched tether cable. A comparatively less dramatic drift is obtained from the side gust, also due to the fact that, when it hits the airship, the latter is displaced downwind (i.e. to the East) of the anchor point with respect to the side wind component blowing from the West.

It can be reported that the results presented herein do not account for ground effect. Testing with a simple model of ground effect have been carried out, simulating the effect with a vertical wind component proportional to the ground speed and to the altitude from the ground. These simulations show that ground effect has generally a mitigating effect on the tension, bearing a result which is however negligible for the lower wind speeds, and slight for an extreme speed of 12 m/s (the difference with respect to the results presented here on the peak tension without ground effect is below 1% for 6 and 9 m/s, and below 8% for 12 m/s).

4.2. Heading control layer

To mitigate the misalignment issues inducing excessive tension values in the scenario described in the previous paragraph (Section 4.1), a heading control system has been implemented, based on a measure of the horizontal misalignment between the position vector from the anchor point $\boldsymbol{AP}_1$ (i.e. the origin of the ground reference) and the tether point $\boldsymbol{TP}_1$, and the longitudinal axis of the airship $\boldsymbol{b}_1$. Both are projected on the plane of the horizon (practically possible by measuring the Euler parameters $\boldsymbol{e}^{\mathcal{B}}_{321}$ of the airship), allowing the definition of the angle χ between them, assumed positive when the target point is to the left of the airship. A simple proportional law is employed to annihilate the misalignment by action of the forward-pointing side thrusters #5, #6, yielding (positive gain κ_χ, see Appendix)

$$\begin{aligned} \Delta\delta^{\chi}_{T_5} &= -\kappa_\chi \chi, \\ \Delta\delta^{\chi}_{T_6} &= +\kappa_\chi \chi. \end{aligned} \tag{42}$$

Fig. 13 and Table 4 display performance indices similar to Fig. 12 and Table 3 respectively, when both the rewind control and the misalignment control are active.

The advantage provided by this additional layer of control is apparent. The tension is clearly reduced with respect to the previous case, as indicated by all indices at every wind speed, yet more markedly at the higher values of the latter. However, for the top considered value of velocity, also this controller fails to keep the tension below the assumed envelope tear strength. Where this is a rather conservative value pertaining to the envelope material only and without accounting for any special reinforcement (as said), this performance is an indication of a possible criticality. Considering the trajectory at 12 m/s (plots in Fig. 13), the misalignment controller allows for a significant reduction of the side-slip effect experienced in the previous case (Fig. 12) as a result of a polluted initial condition. The sideward gust causes some East-bound displacement, producing the elongation to approach unity soon after $t = 20$ s. However, notably more numerous and intense peaks are obtained as a result of a high elongation towards the end of the maneuver, when the tether is approaching its target length of 1.5 m.

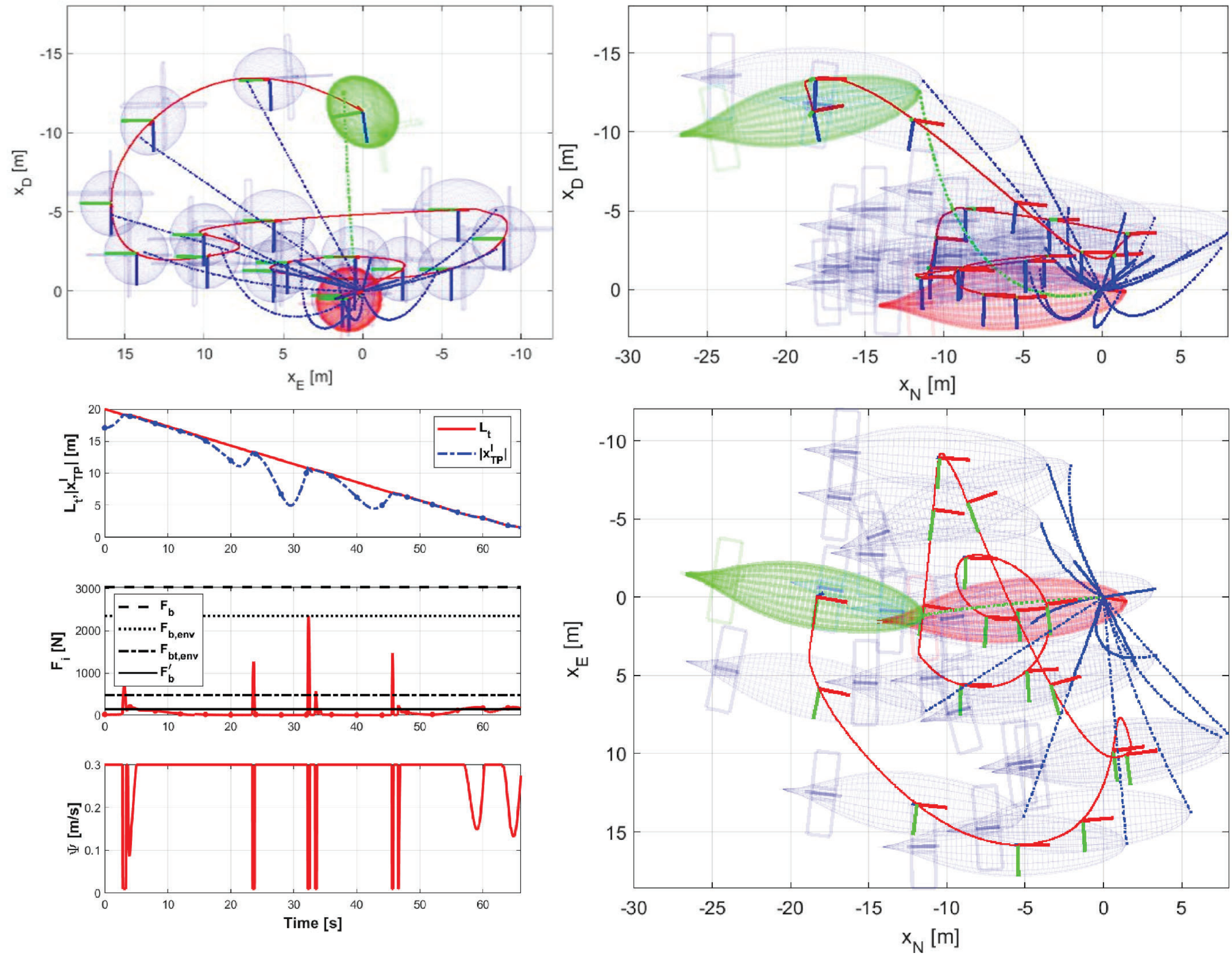

Fig. 12. Trajectory and attitude of the airship in docking with tether rewind control activated. Wind from North at 12 m/s, side gust of 4 m/s @ $t = 20$ s. Snapshots every 4 s. Top-left: View from North. Top-right: View from East. Bottom-right: View from top. Green airship mock-up: Start time of simulation. Red airship mock-up: End time of simulation. Red line on trajectory plots: Trajectory of buoyancy center $\boldsymbol{B}$. Blue dashed line on trajectory plots: Tether cable. Bottom-left plot: Time histories of tether length, tension and rewind rate. (For interpretation of the references to color in this figure legend, the reader is referred to the web version of this article.)

Table 3
Results of the analysis of the time histories of tension at the tether point $\boldsymbol{TP}_1$ for increasing wind speed, with the rewind control active.

Wind [m/s]	Max.$\lvert \boldsymbol{F}_i \rvert$ [N]	Avg.$\lvert \boldsymbol{F}_i \rvert$ [N]	min Ψ [m/s]	$\Delta t_{F'_b}$ [s]	$\Delta t_{F_{bt,env}}$ [s]	$\Delta t_{F_{b,env}}$ [s]	Δt_{F_b} [s]	Δt [s]
6	283	75	0.01	5.18	0	0	0	62.05
9	1,555	51	0.01	3.75	0.28	0	0	62.85
12	2,357	75	0.01	10.77	1.33	0.03	0	66.07

This suggests that by keeping the cable in a low-elongation condition is more critical when the maneuver is coming to a close, corresponding to the shortest values of the cable length.

4.3. Navigation towards the anchor point

Better results than with the control suite developed up to here can be obtained adding a control layer capable of carrying out a near-hover navigation task, where the horizontal and vertical distances of the tether point $\boldsymbol{TP}_1$ from the target anchor point $\boldsymbol{AP}_1$ are targeted. In particular, in the longitudinal direction, thrusters #1, #5, #6 are employed to target the positional error ε_{lon} along the projection of $\boldsymbol{b}_1$ on the horizontal plane (i.e., the plane normal to $\boldsymbol{i}_3$). In addition, as typical to navigation problems, an error on velocity is computed based on the actual ground speed component along $\boldsymbol{b}_1$, namely U, and a corresponding set-point of longitudinal speed $\bar{U}$. The latter is defined as a linear function of the longitudinal positional error ε_{lon}, bounded between a minimum $\bar{U}_{\min}$ and a maximum $\bar{U}_{\max}$. The vertical control acts in a totally similar fashion, employing thrusters #2, #3, #4 to target the positional error ε_{ver} and a vertical velocity setpoint defined in terms of the rate of climb $\overline{RoC}$, i.e. the component of the ground velocity normal to the horizon (i.e., $RoC = -v^{\mathcal{I}}_{B_3}$). This set point is defined as a linear function of ε_{ver}, bounded between a minimum $\overline{RoC}_{\min}$ and a maximum $\overline{RoC}_{\max}$. The resulting control laws can be written as (all gains are positive, see

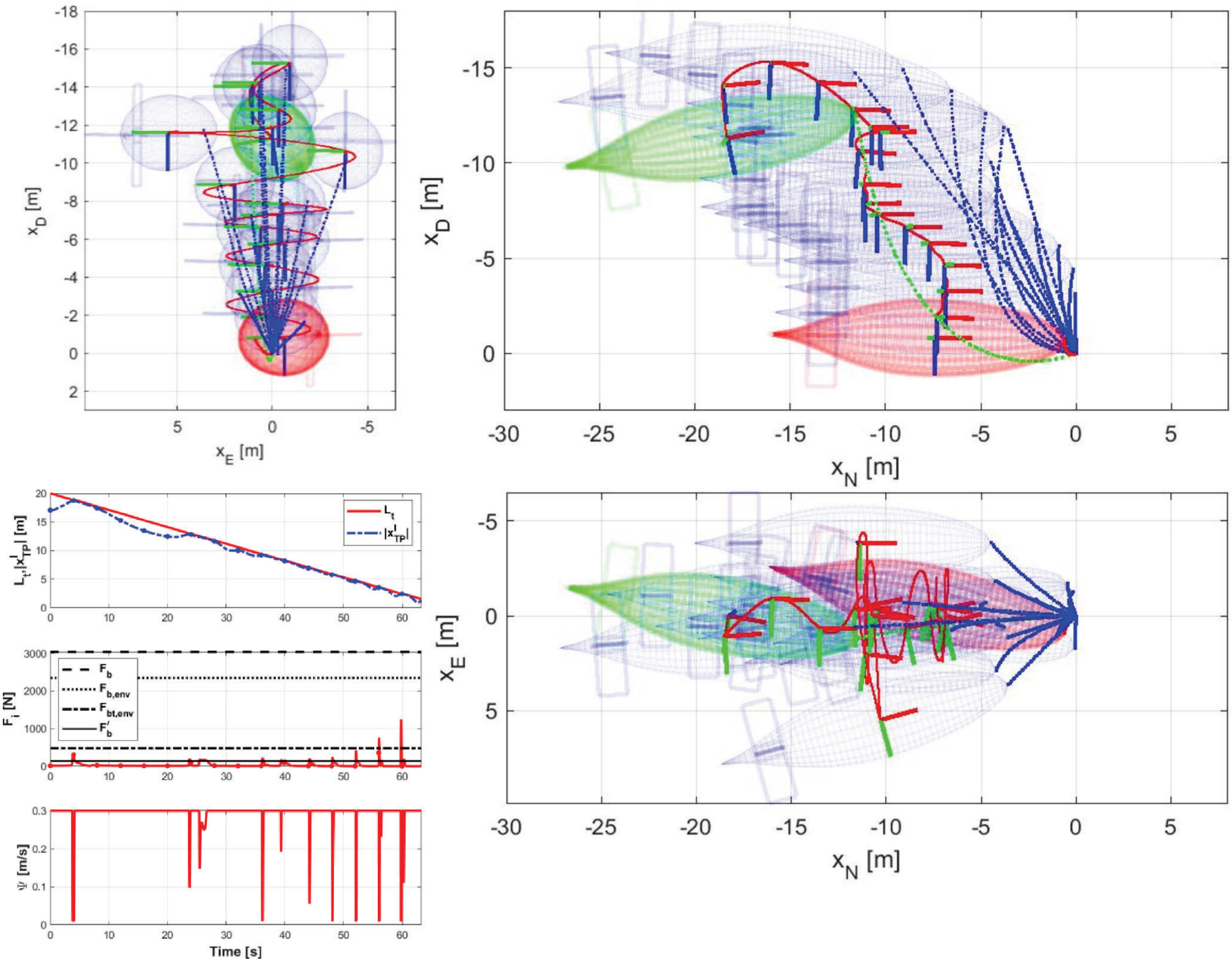

Fig. 13. Trajectory and attitude of the airship in docking, with tether rewind control and an additional misalignment control layer. Same testing conditions and plot settings of Fig. 12.

Table 4
Results of the analysis of the time histories of tension at the tether point $\boldsymbol{TP}_1$ for increasing wind speed, with the rewind control and misalignment control both active.

Wind [m/s]	Max.$\|\boldsymbol{F}_i\|$ [N]	Avg.$\|\boldsymbol{F}_i\|$ [N]	min Ψ [m/s]	$\Delta t_{F'_b}$ [s]	$\Delta t_{F_{bt,env}}$ [s]	$\Delta t_{F_{b,env}}$ [s]	Δt_{F_b} [s]	Δt [s]
6	156	66	0.30	0.15	0	0	0	61.67
9	191	38	0.15	0.50	0	0	0	62.00
12	1,246	33	0.01	4.075	0.25	0	0	63.27

Appendix)

$$\begin{aligned}
&\Delta\delta_{T_i} = -\kappa_{hor}\epsilon_{hor} + \kappa_U(U - \bar{U}),\ i = 1, 3, 4,\\
&\Delta\delta_{T_i} = -\kappa_{ver}\epsilon_{ver} + \kappa_{RoC}(RoC - \overline{RoC}),\ i = 2,\\
&\Delta\delta_{T_i} = +\kappa_{ver}\epsilon_{ver} - \kappa_{RoC}(RoC - \overline{RoC}),\ i = 4, 5.
\end{aligned} \tag{43}$$

Both the extreme values of $\bar{U}$ and $\overline{RoC}$ have been set to 0.5 m/s. The action of the navigation controller is designed to work synergistically with the other layers. In particular, the airship should keep horizontal in attitude (through the action of the SAS/attitude control) and aligned with the direction of the target point (through the action of the heading control layer). Similar to the previous cases, Fig. 14 and Table 5 display the results obtained with this additional control layer, considering in particular a wind speed of 12 m/s in the figures.

Looking at the latter, the airship tends to shift forward from the start, as a result of positional control. The docking maneuver is then mostly vertical, assisted by the slow downward motion of the vertical navigation layer, which allows keeping the cable to an elongation slightly below unity, and helps avoiding the bounce effect which produces tension peaks. As a matter of fact, the tension never reaches the tear stress even in the most demanding scenario (i.e., 12 m/s), whereas for lower wind speeds (Table 5) the rewind controller never triggers a reduction of the rewind rate Ψ.

For a more convenient at-a-glance comparison of the results of the simulations presented in this section, a three-quarter view of the corresponding trajectories is presented in Fig. 15 (referring respectively to Figs. 12–14).

With an understanding of the performance of the three controllers, it is interesting to quickly check the results in a comparative fashion, in-

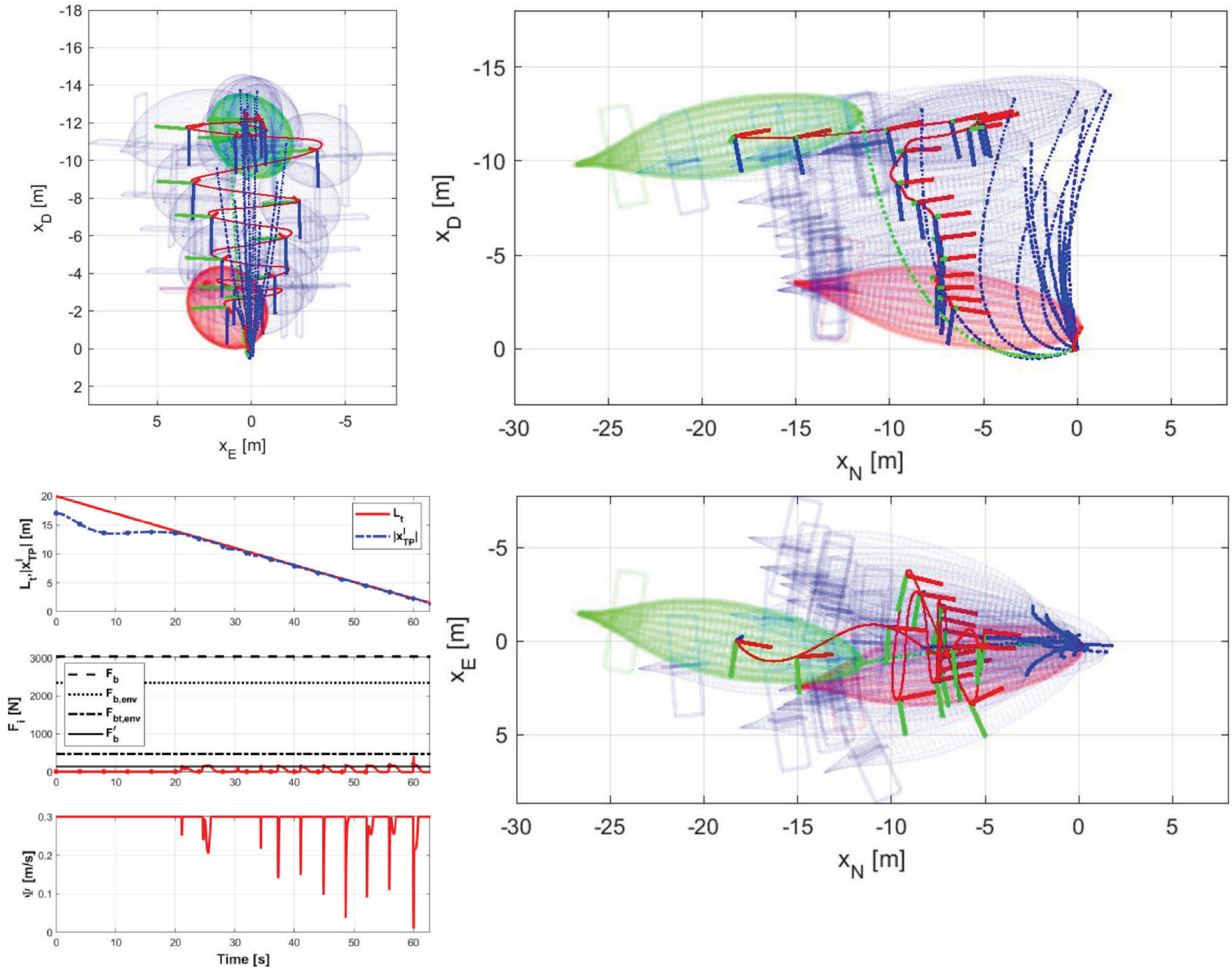

Fig. 14. Trajectory and attitude of the airship in docking, with misalignment and navigation layers all active. Same testing conditions and plot settings of Fig. 12.

Table 5
Results of the analysis of the time histories of tension at the tether point $\boldsymbol{TP}_1$ for increasing wind speed, with the rewind, misalignment and navigation control layers all active.

Wind [m/s]	Max.$\lvert \boldsymbol{F}_i \rvert$ [N]	Avg.$\lvert \boldsymbol{F}_i \rvert$ [N]	min Ψ [m/s]	$\Delta t_{F'_b}$ [s]	$\Delta t_{F_{bt,env}}$ [s]	$\Delta t_{F_{b,env}}$ [s]	Δt_{F_b} [s]	Δt [s]
6	14	6	0.30	0	0	0	0	61.67
9	15	7	0.30	0	0	0	0	61.67
12	422	41	0.01	7.00	0	0	0	62.86

Table 6
Control usage and effectiveness parameters, computed for the three considered control layers and for different values of the wind speed.

	ADC [-]			E_{δ_T} [-]			ϑ_{RMS} [deg]		
	6 m/s	9 m/s	12 m/s	6 m/s	9 m/s	12 m/s	6 m/s	9 m/s	12 m/s
Rewind (SAS only on airship)	0.11	0.25	0.58	0.45	0.42	0.69	4.92	2.74	3.30
Rewind, heading	0.16	0.39	0.69	0.45	0.67	0.95	4.98	3.35	2.44
Norm. Δ vs. Rewind	+46.9%	+54.3%	+19.6%	−0.2%	+61.3%	+37.7%	+1.32%	+22.2%	−25.8%
Rewind, heading, navigation	0.12	0.31	0.94	0.21	0.68	1.51	2.16	4.97	8.04
Norm. Δ vs. Rewind	+9.4%	+24.9%	+62.2%	−53.0%	+62.6%	+117.9%	−56.2%	+81.4%	+143.5%

cluding additional measures of performance. The control effort is measured firstly through an actuator duty cycle (ADC) for all thrusters, defined as $ADC = \sum_{i=1}^{N_T} \frac{1}{t_f - t_0} \int_{t_0}^{t_f} \left| \frac{\mathrm{d}\delta_{T_i}}{\mathrm{d}t} \right| \mathrm{d}t$. In a similar fashion, the energy spent in the control action of all actuators is computed as the integral $E_{\delta_T} = \sum_{i=1}^{N_T} \frac{1}{t_f - t_0} \int_{t_0}^{t_f} \left| \delta_{T_i} \right| \mathrm{d}t$, for each control option and wind speed. Finally, the ability of the controller in conditioning the motion of the airship is measured by computing the root mean square value of the pitch angle of the airship, ϑ_{RMS}, which should be ideally driven to zero. A comparison of these indices is reported in Table 6, showing values pertaining to different control options and for each wind speed, as well as normalized percent changes with respect to the pure rewind control case

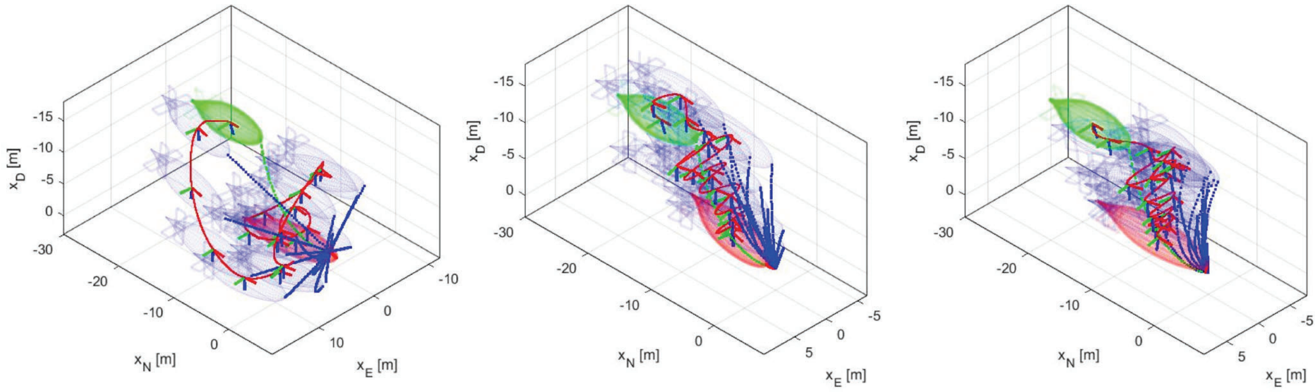

Fig. 15. Comparison of three-quarter views of the trajectory of the airship and evolution of the configuration of the cable, for the same cases portrayed in Figs. 12–14, respectively from left to right.

(Section 4.1), where the control of the thrusters is only governed by the stability augmentation layer.

Clearly, an increase in the travel of the of thrust control signals is in order when additional control layers making use of these controls are activated. This is witnessed by the increase in ADC when activating the directional and navigational layers. The trend for 6 and 9 m/s appears to show a more efficient use of control with the navigation layer working, whereas the navigation layer imposes an increase on ADC at 12 m/s. This suggests that a retuning of the controller gains (not implemented) may be advisable when moving to these extreme wind speeds. The energy indicator E_{δ_T} provides a similar picture, with the peculiarity that for 6 m/s the required control energy is reduced with respect to the baseline controller (even though the ADC is not, as seen). To explain this, it should be pointed out that this parameter is sensitive to the trim value of the thrust setting (initial value). The actual unfolding of the simulation, following the initial perturbation and depending on the target of the control action, can in principle induce a reduction of all thrust settings, thus in turns causing a reduction in the overall control energy value. Finally, the ability of the controller to keep the machine close to its target ϑ value does not follow a clear trend. It should be noted that this performance index measures mostly the ability of the stability augmentation layer, which targets ϑ, in conjunction with the other control layers (see Eq. (40)). Furthermore, despite the seemingly striking percentage difference, the value of ϑ remains generally limited (the worst case is represented by the simulation portrayed in Fig. 14, and on the rightmost plot of Fig. 15).

Besides complementing the analysis of the control performance on the tension, previously shown, the performance indices in Table 6 allows ascertaining that the control action remains generally limited, and compatible with a physical behavior of the actuators, which are fast-reacting, small servo-electric motors. Moreover, the absence of saturation phenomena in all time histories of control has been checked visually.

5. Conclusion

As mentioned in the introduction (Section 1), this research has served two major aims. Firstly, it has introduced and demonstrated a useful tool for the design and testing of airships, inclusive of a realistic model of a tethering cable. In facts, after introducing a model for airship flight dynamics such to cope with the presence of a tethering system, a model for a tether cable has been presented, obtained from elaboration of pre-existing models and adapted by employing a careful tensor representation to work in a completely general, three-dimensional environment. This model has been plugged in to the airship model, producing a mid-fidelity model of a tethered airship. Then a rigorous procedure for the linearization of the equations for dynamic equilibrium of a tethered airship has been developed, notably such to enable the writing of the equations of motion at whatever point (thus sufficiently general to be potentially applicable also to describe the dynamics of other tethered vehicles, e.g., aircraft, submarines, etc.).

Secondly, the integrated airship/tether cable model has been employed to analyze a realistic scenario, considering a small-scale unmanned airship in a tethered docking maneuver, thus proving the sensitivity and suitability of the proposed model as a tool for airship design and control testing. To this aim, a starting condition of a docking maneuver has been selected in the form of a trimmed solution where the machine is standing still with respect to the ground, in presence of a horizontal wind, with thrusters running and a tether cable linked to the ground.

This reference condition has been employed in a first stage for carrying out linear analyses in a parameterized fashion. Positional states are included in the analysis, together with usual body components of velocity, rotational rate and Euler parameters of the airship (as typical to trim in free flight). An analysis for changing values of characteristics of the cable, has allowed to show that the eigenvalues induced in this static equilibrium problem by the additional positional states keep a globally low frequency, yet display a rather complex behavior, which may configure subsidence or oscillatory modes involving longitudinal motion. These depend from the weight and diameter of the tether, when considering a single cable. The longitudinal mode just mentioned is obtained by the interplay between the original (untethered) surge mode and a mostly longitudinal motion (i.e. in the direction of the wind and plane of symmetry of the airship, in the considered scenario). An oscillatory lateral-directional motion is obtained for sufficiently heavy/thick cables, when considering an alternative configuration with two tethering cables. For positions of the tether attachment on board shifting backwards (towards the tail of the airship), when considering again a single tether cable configuration, an oscillatory lateral-directional mode may be induced by the interplay between a directional mode associated to yaw (originally a null mode in calm air) and a mostly cross-wind lateral-directional mode imported by the presence of positional states. This oscillatory mode is marginally stable, whereas a vertical translation subsidence mode results unstable for a positioning of the tether point sufficiently close to the tail. Additionally, the wind intensity appears to play a rather different role especially on pendulum oscillation with respect to an untethered condition, bearing a break-down of this mode into two longitudinal subsidence modes, for a sufficiently high intensity of the wind. Globally however, the free response of the considered airship and flight conditions, idealized yet sufficiently realistic for representing the starting condition of a docking maneuver, does not seem to pose significant issues for a standard flight controller, since no fast instability arises. This is especially true when employing thrusters for control, which by design (i.e., for a suitable layout of the thrusters) allow for a more accurate injection of control action, with respect to aerodynamic surfaces (even more so, at low dynamic pressure values close to hovering flight).

Then in the final stage of this research, three controllers of increasing complexity have been employed to carry out a simulated docking maneuver. These are based respectively on a modulated rewind action based on the tension value, on an additional layer targeting horizontal misalignment between the airship longitudinal axis and the target point on ground, and on a further near-hover three-dimensional navigation controller. Testing was carried out starting from a trimmed condition, perturbed in all attitude angles, for a horizontal wind of different intensity and including a side gust. As performance parameters, the tension at the tether point as well as the duration of the maneuver are considered. This realistic type of maneuver has been inspired by a potential certification testing in docking, which is still to be defined for the class of lightweight unmanned airships of interest in this work. It can be observed that, as expected, the three controllers perform increasingly well, at the price of additional complexity, related cost of the sensor suite, and an additional burden on the actuators (i.e. the motors) especially for extreme wind speeds.

Larger-scale employment of this model in future research shall entail the inclusion of tethered maneuvers in a design-for-certification framework, expanding the scope of the most modern methodologies for airship design by including relevant cases like tethered docking in the airship sizing loop [55].

CRediT authorship contribution statement

Carlo E.D. Riboldi: Writing – review & editing, Writing – original draft, Visualization, Supervision, Software, Methodology, Investigation, Formal analysis, Data curation, Conceptualization; **Alessandro Croce:** Writing – review & editing, Supervision, Methodology, Investigation, Formal analysis, Data curation, Conceptualization; **Francesco A.C. Pagani:** Validation, Software, Investigation, Data curation; **Hui He:** Validation, Software, Investigation, Data curation; **Giorgio Bortolini:** Validation, Software, Investigation, Data curation.

Funding

This research did not receive any specific grant from funding agencies in the public, commercial, or not-for-profit sectors.

Declaration of competing interest

The authors declare that they have no known competing financial interests or personal relationships that could have appeared to influence the work reported in this paper.

Data availability

Data will be made available on request.

Appendix A. Control settings

The parameters employed for the controllers in the simulations presented in Section 4 are reported in the following Tables A.1–A.4.

Table A.1
Control settings for stability augmentation system (SAS, see Eq. (40)).

k_q^{SAS}	1.0 1/(rad/s)		
k_ϑ	0.5 1/rad	$\bar{\vartheta}$	0 deg
k_p^{SAS}	2.0 1/(rad/s)		
k_φ	0.5 1/rad	$\bar{\varphi}$	0 deg
k_r^{SAS}	5.0 1/(rad/s)		

Table A.2
Control settings for rewind control system (see Eq. (41)).

k_Ψ	0.005 m/(s·N)
$\bar{\Psi}$	0.3 m/s
F_i'	144.3 N
$\Psi_{\min}$	0.01 m/s

Table A.3
Control settings for heading control layer (see Eq. (42)).

k_χ	5.0 1/rad

Table A.4
Control settings for heading control layer (see Eq. (43)).

k_{hor}	0.0033 1/m		
k_U	0.033 1/(m/s)	$\max\lvert\bar{U}\rvert$	0.5 m/s @ 5.0 m hor. displ. error
k_{ver}	0.0033 1/m		
k_{RoC}	0.033 1/(m/s)	$\max\lvert\overline{RoC}\rvert$	0.5 m/s @ 5.0 m ver. displ. error

References

[1] C.E.D. Riboldi, L. Fanchini, Assessing the technical–economic feasibility of low-altitude unmanned airships: methodology and comparative case studies, Aerospace 12 (2025) 244. https://doi.org/10.3390/aerospace12030244
[2] SCEYE Inc., 50 George Applebay Way, Building 200, Moriarty, NM 87035, USA - sceye.com, accessed Feb. 2026.
[3] C.E.D. Riboldi, A. Rolando, Layout analysis and optimization of airships with thrust-based stability augmentation, Aerospace 9 (2022) 393. https://doi.org/10.3390/aerospace9070393
[4] C.E.D. Riboldi, A. Rolando, Thrust-based stabilization and guidance for airships without thrust-vectoring, Aerospace 10 (2023). https://doi.org/10.3390/aerospace10040344
[5] C.E.D. Riboldi, A. Rolando, Autonomous flight in near hover and hover for thrust controlled unmanned airships, Drones 7 (2023). https://doi.org/10.3390/drones7090545
[6] Kelluu Oy, Metallimiehentie 4, 80330 Reijola, Finland - kelluu.com, accessed Feb. 2026.
[7] FloFleet, Via Sebenico 24, 20124 Milan, Italy - www.flofleet.com, accessed Feb. 2026.
[8] Roboloon, Nobelstraße 15, 70569 Stuttgart, Germany - www.roboloon.com, accessed Feb. 2026.
[9] S. Miller, R. Fesen, L. Hillenbrand, J. Rhodes, Airships: A New Horizon for Science, Tech. rep., The Keck Institute for Space Studies, 2014.
[10] Q. Wang, J. Chen, G. Fu, D. Duan, H. Zhao, A methodology for optimisation design and analysis of stratosphere airship, Aeronaut. J. 113 (1146) (2009) 533–540. https://doi.org/10.1017/S0001924000003183
[11] X. Yang, D. Liu, Conceptual design of stratospheric airships focusing on energy balance, J. Aerosp. Eng. 31 (2018). https://doi.org/10.1061/(ASCE)AS.1943-5525.0000814
[12] L. Zhang, W. Zhu, H. Du, M. Lv, Multidisciplinary design of high altitude airship based on solar energy optimization, Aerosp. Sci. Technol. 110 (106440) (2021). https://doi.org/10.1016/j.ast.2020.106440
[13] C.E.D. Riboldi, A. Rolando, G. Regazzoni, On the feasibility of a launcher-deployable high-altitude airship: effects of design constraints in an optimal sizing framework, Aerospace 9 (2022) 1–37. https://doi.org/10.3390/aerospace9040210
[14] C.E.D. Riboldi, A. Rolando, S. Cacciola, G. Regazzoni, I. Spadafora, On the optimal preliminary design of high-altitude airships: automated procedure and the effect of constraints, in: Aerospace Europe Conference 2023 - 10th EUCASS - 9th CEAS, 9-13 July 2023, Lausanne, Switzerland, 2023, pp. 1–15.
[15] C.E.D. Riboldi, M. Belan, S. Cacciola, R. Terenzi, S. Trovato, D. Usuelli, G. Familiari, Preliminary sizing of high-altitude airships featuring atmospheric ionic thrusters: an initial feasibility assessment, Aerospace (2024). https://doi.org/10.3390/aerospace11070590
[16] C.E.D. Riboldi, M. Belan, S. Cacciola, R. Terenzi, S. Trovato, D. Usuelli, G. Familiari, Preliminary sizing of a low-altitude airship including ion-plasma thrusters, in: 34th Congress of the International Council of the Aeronautical Sciences (ICAS2024), 9-13 September 2024, Florence, Italy, 2024, pp. 1–20.
[17] C.E.D. Riboldi, M. Belan, R. Terenzi, Q. Zhao, Optimal topology of a small-scale airship: a study in virtual environment, in: 11th European Conference for AeroSpace Sciences (EUCASS 2025), 30 Jun.-4 Jul. 2025, Rome, Italy, 2005, pp. 1–13.
[18] S.P. Jones, J.D. DeLaurier, Aerodynamic estimation techniques for aerostats and airships, J. Aircr. 20 (2) (1982) 120–126.
[19] M.B. Tischler, R.R. Ringland, H.R. Jex, Heavy airship dynamics, J. Aircr. 20 (1983) 425–433.
[20] B. Kämpf, Flugmechanik und Flugregelung von Luftschiffen, Ph.D. thesis, University of Stuttgart, 2004. https://doi.org/10.18419/opus-3715

[21] Y. Li, M. Nahon, Modeling and simulation of airship dynamics, J. Guid. Control Dyn. 30 (2007) 1691–1700.
[22] Y. Li, M. Nahon, I. Sharf, Dynamics modeling and simulation of flexible airships, AIAA J. 47 (2009) 592–605. https://doi.org/10.2514/1.37455
[23] M.M. Munk, The Aerodynamic Forces on Airship Hulls, Tech. rep., National Advisory Committee for Aeronautics, 1924. TR-184.
[24] S.F. Hoerner, Fluid-Dynamic Drag, Hoerner Fluid Dynamics, 1965.
[25] A.B. Wardlaw, High Angle of Attack Missile Aerodynamics, Tech. rep., AGARD Lecture Series 98, 1979.
[26] A. Kornienko, System Identification Approach for Determining Flight Dynamical Characteristics of an Airship from Flight Data, Ph.D. thesis, University of Stuttgart, 2006. https://doi.org/10.18419/opus-3731
[27] L. Chen, L. Huang, J. Lin, Servo-elastic control of a flexible airship with multiple vectored propellers, Aerospace 13 (3) (2026). https://doi.org/10.3390/aerospace13030275
[28] Z. Song, L. Chen, X. Wang, Flight control for a flexible airship with servo-elastic suppression, Aerosp. Syst. (2026) 1–11. https://doi.org/https://doi.org/10.1007/s42401-026-00479-w
[29] L. Beji, A. Abichou, Tracking control of trim trajectories of a blimp for ascent and descent flight manoeuvres, Int. J. Control 78 (10) (2005) 706–719.
[30] Z. Cai, W. Qu, Y. Xi, Y. Wang, Stabilization of an underactuated bottom-heavy airship via interconnection and damping assignment, Int. J. Robust Nonlinear Control 17 (18) (2007) 1690–1715.
[31] E. Paiva, F. Benjovengo, S. Bueno, P. Ferreira, Sliding mode control approaches for an autonomous unmanned airship, in: 18th AIAA Lighter-Than-Air Systems Technology Conference, 4-7 May 2009, Seattle, WA, 2009, pp. 1–12.
[32] T. Liesk, M. Nahon, B. Boulet, Design and experimental validation of a nonlinear low-level controller for an unmanned fin-less airship, IEEE Trans. Control Syst. Technol. 21 (1) (2013) 149–161.
[33] Y. Yang, J. Wu, W. Zheng, Station-keeping control for a stratospheric airship platform via fuzzy adaptive backstepping approach, Adv. Space Res. 51 (7) (2013) 1157–1167.
[34] Y. Yang, J. Wu, W. Zheng, Positioning control for an autonomous airship, J. Aircr. 53 (6) (2016) 1638–1646.
[35] J.S. Santos, S. Stevanovic, K. Kondak, F. Holzapfel, L.C. Góes, R.S. Pant, Stability augmentation system for a tethered airship, in: 16th AIAA Aviation Technology, Integration, and Operations Conference, 13-17 June 2016, Washington, D.C., 2016, p. 4224.
[36] Many Authors, Low-Altitude LTA UAS Task Force Proposition for the Revision of SORA 2.5, Tech. Rep., U-LTA - Upscaling of Lighter-Than-Air, 2026.
[37] J.D. DeLaurier, A stability analysis for tethered aerodynamically shaped balloons, J. Aircr. 9 (9) (1972) 646–651.
[38] J.D. DeLaurier, Prediction of tethered-aerostat response to atmospheric turbulence, J. Aircr. 14 (4) (1977) 407–409.
[39] S.P. Jones, J.A. Krausman, Nonlinear dynamic simulation of a tethered aerostat, J. Aircr. 19 (8) (1982) 679–686.
[40] D. Humphreys, Validation of the dynamic characteristics of a towed, scaled aerostat, in: 12th Lighter-Than-Air Systems Technology Conference, 3-5 June 1997, San Francisco, CA, 1997, p. 1486.
[41] S.P. Jones, L.D. Schroeder, Nonlinear dynamic simulation of a tethered aerostat: a fidelity study, J. Aircr. 38 (1) (2001) 64–68.
[42] C. Lambert, M. Nahon, Stability analysis of a tethered aerostat, J. Aircr. 40 (2003) 705–715.
[43] R. Kumar, S. Srivastava, A.K. Ghosh, B. Gupta, A. Kumar, Parametric trend study during stability analysis of a tethered aerostat, J. Aerosp. Sci. Technol. (2011) 107–124.
[44] N. Bigi, A. Nême, K. Roncin, J.-B. Leroux, G. Bles, C. Jochum, Y. Parlier, Airborne Wind Energy, Springer Nature Singapore Pte. Ltd., 2018, pp. 57–78 Ch. 3. Analytical Tether Model for Static Kite Flight.
[45] D.F. Duda, H. Fuest, T. Islam, T. Ostermann, D. Moormann, Hybrid modeling approach for the tether of an airborne wind energy system, CEAS Aeronaut. J. 13 (2022) 627–637. https://doi.org/10.1007/s13272-022-00581-7
[46] B.N. Pamadi, Performance, Stability, Dynamics, and Control of Airplanes, AIAA Education Series, American Institute of Aeronautics and Astronautics, Inc., 2004.
[47] C.E.D. Riboldi, Flight Dynamics: Modeling, Characterization and Performance, Esculapio, Bologna, Italy, 2024.
[48] Tecnofuni s.n.c., via Pastore 3, 15076 Ovada (AL), Italy - www.tecnofuni.com, Catalogo Funi Tessili, accessed Sep. 2025.
[49] Marlow ropes Ltd, Ropemaker Park, Diplocks Way, Hailsham, East Sussex BN27 3GU UK - www.marlowropes.com, accessed Oct. 2025.
[50] Orcina, Daltongate, Ulverston, Cumbria LA12 7AJ UK - www.orcina.com, OrcaFlex (v11.6c) User's manual, accessed Oct. 2025.
[51] C.E.D. Riboldi, M. Tomasoni, Formation flight of fixed-wing UAVs: dynamic modeling, guidance design, and testing in realistic scenarios, Aerospace 12 (2025) 260. https://doi.org/10.3390/aerospace12030260.
[52] IPROP - Ionic Propulsion in the Atmosphere - www.iprop-project.eu, Grant ID: HORIZON-EIC-2022-PATHFINDEROPEN-01, 2023-2027.
[53] Mehler Texnologies GmbH, Rheinstrasse, 41836 Hückelhoven, Germany - www.mehler-texnologies.com, accessed Jan. 2026.
[54] South Pacific Grand Winches Industry, CO, LTD., No. 42, Fuxing Rd., Longtan District, Taoyuan City, 325. Taiwan. www.southpacific.com.tw, Winch series 800/900, accessed May 2026.
[55] C.E.D. Riboldi, L. Alessi, R. Terenzi, Airship sizing for flying qualities: an automated methodology and applications, J. Aircr. (article in progress, available online) (2026). https://doi.org/10.2514/1.C038971.